Monthly Notices
of the
ROYAL ASTRONOMICAL SOCIETY

MNRAS **468,** 2532–2551 (2017)
Advance Access publication 2017 March 16

doi:10.1093/mnras/stx653

Probing the interstellar dust towards the Galactic Centre: dust-scattering halo around AX J1745.6−2901

Chichuan Jin,[1]★ Gabriele Ponti,[1] Frank Haberl[1] and Randall Smith[2]

[1]*Max-Planck-Institut für Extraterrestrische Physik, Giessenbachstrasse, D-85748 Garching, Germany*
[2]*Smithsonian Astrophysical Observatory, 60 Garden Street, Cambridge, MA 02138, USA*

Accepted 2017 March 13. Received 2017 March 13; in original form 2016 November 7

ABSTRACT

AX J1745.6−2901 is an X-ray binary located at only 1.45 arcmin from Sgr A⋆, showcasing a strong X-ray dust-scattering halo. We combine *Chandra* and *XMM–Newton* observations to study the halo around this X-ray binary. Our study shows two major thick dust layers along the line of sight (LOS) towards AX J1745.6−2901. The LOS position and $N_{\rm H}$ of these two layers depend on the dust grain models with different grain size distributions and abundances. But for all the 19 dust grain models considered, dust layer-1 is consistently found to be within a fractional distance of 0.11 (mean value: 0.05) to AX J1745.6−2901 and contains only (19–34) per cent (mean value: 26 per cent) of the total LOS dust. The remaining dust is contained in layer-2, which is distributed from the Earth up to a mean fractional distance of 0.64. A significant separation between the two layers is found for all the dust grain models, with a mean fractional distance of 0.31. Besides, an extended wing component is discovered in the halo, which implies a higher fraction of dust grains with typical sizes $\lesssim$590 Å than considered in current dust grain models. Assuming AX J1745.6−2901 is 8 kpc away, dust layer-2 would be located in the Galactic disc several kpc away from the Galactic Centre (GC). The dust scattering halo biases the observed spectrum of AX J1745.6−2901 severely in both spectral shape and flux, and also introduces a strong dependence on the size of the instrumental point spread function and the source extraction region. We build XSPEC models to account for this spectral bias, which allow us to recover the intrinsic spectrum of AX J1745.6−2901 free from dust-scattering opacity. If dust layer-2 also intervenes along the LOS to Sgr A⋆ and other nearby GC sources, a significant spectral correction for the dust-scattering opacity would be necessary for all these GC sources.

Key words: dust, extinction – Galaxy: centre – X-rays: binaries – X-rays: ISM.

1 INTRODUCTION

The centre of the Milky Way (i.e. the Galactic Centre, hereafter GC) is one of the most attractive regions for astrophysical studies. It has been observed that thousands of point-like X-ray sources and extended sources are sitting in this region (e.g. Wang, Gotthelf & Lang 2002; Muno et al. 2003, 2005, 2009; Degenaar et al. 2012, 2015; Ponti et al. 2015b, 2016), including Sgr A⋆ that is the supermassive black hole closest to Earth (e.g. Genzel, Eisenhauer & Gillessen 2010). The inner few hundred parsecs contain a large concentration of molecular material (e.g. Morris & Serabyn 1996), which is revealing traces of previous active periods of Sgr A⋆ (see Ponti et al. 2013, for a review). However, the GC region is also highly extincted from the optical to the soft X-ray band (e.g. Becklin & Neugebauer 1968; Fritz et al. 2011), elevating the importance of understanding the properties of gas and dust in front of the GC.

⋆E-mail: chichuan@mpe.mpg.de

Previous studies about the diffuse emission and point sources around the GC line of sight (LOS) often suggest a large hydrogen column density of $N_{\rm H} \gtrsim 10^{22}$ cm^{-2}, as measured by absorption models in the X-ray spectral fitting (hereafter $N_{\rm H,\,abs}$; e.g. Terrier et al. 2010; Molinari et al. 2011; Degenaar et al. 2012). The large $N_{\rm H,\,abs}$ also implies a large dust column assuming typical gas-to-dust ratios (e.g. Predehl & Schmitt 1995). Recently, several papers show that dust scattering can have a significant impact on the observed X-ray spectra (Smith, Valencic & Corrales 2016), causing significant bias to $N_{\rm H,\,abs}$ if the dust-scattering opacity is not properly considered in the spectral fitting (Corrales et al. 2016). Therefore, it is especially important to consider the effects of dust scattering when studying X-ray sources in the GC direction.

1.1 Dust-scattering halo in X-rays

The idea that dust grains along the LOS can produce an observable halo around X-ray sources, the so-called 'dust-scattering halo', was proposed 50 yr ago (Overbeck 1965; Trümper & Schönfelder 1973)

© 2017 The Authors
Published by Oxford University Press on behalf of the Royal Astronomical Society

Downloaded from https://academic.oup.com/mnras/article/468/3/2532/3072846 by Biblioteca di Scienze tecnologiche user on 30 December 2020

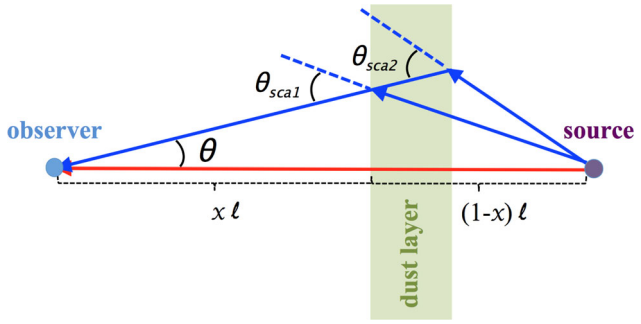


Figure 1. Geometry of the dust scattering by a single thick dust layer. θ is the viewing angle. $\theta_{\rm sca1}$ and $\theta_{\rm sca2}$ are the two scattering angles at the same viewing angle but different locations in the dust layer. ℓ is the absolute distance between the source and the observer, x is the fractional distance from the dust layer to the observer.

and was first observed by the *Einstein* satellite around GX 339−4 (Rolf 1983). The investigation of the dust-scattering halo can provide important information about the location of the dust along the LOS as well as the size and composition of the dust grains (e.g. Predehl et al. 1992; Predehl & Schmitt 1995; Xiang, Zhang & Yao 2005; Valencic & Smith 2015; Heinz et al. 2016; Vasilopoulos & Petropoulou 2016).

1.1.1 *Basic principles of the dust-scattering theory*

We assume a point source that is located at a distance ℓ from the observer characterized by a flux F_X and absorbed by neutral material with a hydrogen column density $N_{\rm H}$. With assumptions made in the dust grain models about the dust-to-gas ratio and abundances, this $N_{\rm H}$ is determined by the total number of dust grains required (hereafter $N_{\rm H,\,sca}$). Moreover, we assume that dust grains are distributed along the LOS with a normalized distribution function $f(x)$ (where x $(0 \leq x \leq 1)$ is the fractional distance between the observer and the dust grains, as drawn in Fig. 1). The intensity of the scattering light at the viewing angle θ, due to a single dust scattering (Mathis & Lee 1991), is given by

$$I^{(1)}_{\rm sca}(\theta) = F_X N_{\rm H,sca} \int_{E_{\rm min}}^{E_{\rm max}} S(E) \int_0^1 \frac{f(x)}{(1-x)^2} \int_{a_{\rm min}}^{a_{\rm max}} n(a) \times \frac{{\rm d}\sigma_{sca}(a,x,E,\theta)}{{\rm d}\Omega}\,{\rm d}a\,{\rm d}x\,{\rm d}E, \quad (1)$$

where $S(E)$, $n(a)$ and $\sigma_{\rm sca}(a, x, E, \theta)$ are the normalized source spectrum, dust grain size distribution and the scattering cross-section, respectively. $n(a)$ depends on the dust grain model and contains assumptions about the abundances and the dust-to-gas ratio. The wavelength of the X-ray photon is much smaller than the typical size range of dust grains in the interstellar medium (ISM), and the refraction index of the dust grain is close to unity. Therefore, the Rayleigh–Gans approximation, instead of a full Mie calculation, can be used to simplify the calculation (e.g. Mathis & Lee 1991). So the differential cross-section can be written as

$$\frac{{\rm d}\sigma_{\rm sca}}{{\rm d}\Omega} = (1.1\,{\rm cm^2\,sr^{-1}}) \left(\frac{2Z}{M}\right)^2 \left(\frac{\rho}{3\,{\rm g\,cm^{-3}}}\right) \left[\frac{F(E)}{Z}\right]^2 \times \left(\frac{a}{1\,\mu m}\right)^6 \Phi^2(a,x,E,\theta), \quad (2)$$

where $\Phi(a, x, E, \theta)$ is the form factor (Bohren & Huffman 1983) that can be approximated by a Gaussian form for a spherical dust grain with both good accuracy and high computing efficiency:

$$\Phi^2(a,x,E,\theta) = \exp\,[-0.4575\ E({\rm keV})^2\ a(\mu{\rm m})^2 \theta_{\rm sca}({\rm arcmin})^2], \quad (3)$$

where the scattering angle $\theta_{\rm sca}$ can be derived from x and θ from simple geometric calculations:

$$\theta_{\rm sca} = \arctan\left(\frac{x}{1-x} \cdot \tan\theta\right) + \theta. \quad (4)$$

The advantage of using the Gaussian approximation is the much higher computing efficiency with good accuracy. Mathis & Lee (1991) compared the scattering profiles between the exact form factor and the Gaussian approximation, and found at most 10 per cent difference at all scattering angles. According to the above equations, we can also define a typical dust grain size for a specific $\theta_{\rm sca}$ as

$$a(\mu m) = \frac{1.4785}{E({\rm keV})\,\theta_{\rm sca}({\rm arcmin})}. \quad (5)$$

Note that for a dust layer with a non-negligible thickness, the scattering light at a specific viewing angle θ comprises a range of scattering angles ($\theta_{\rm sca1} - \theta_{\rm sca2}$, Fig. 1). It can therefore be predicted that the dust scattering from a distinct layer will produce a halo around X-ray sources. Equation (3) indicates that the halo intensity is the strongest in the core and fades out quickly outside a few arcmin, making a point source slightly extended. The typical halo size changes with the photon energy as $\propto\exp(-E^2)$. Therefore, a strong dust-scattering halo is most likely to be observed in the soft X-ray band from a bright X-ray source with a significant amount of intervening dust on the LOS.

Finally, the optical depth of the dust-scattering $\tau_{\rm sca}$ can be estimated from the observation using the fraction of the halo flux ($F_{\rm sca}$) in the total observed flux ($F_{\rm obs}$) (Mathis & Lee 1991; Predehl & Schmitt 1995; Valencic et al. 2009):

$$\tau_{\rm sca} = -\ln(1 - F_{\rm sca}/F_{\rm obs}). \quad (6)$$

1.1.2 *Variability of the dust-scattering halo*

A dust-scattering halo will show variability if the source is variable (Trümper & Schönfelder 1973; Mao, Ling & Zhang 2014; Heinz et al. 2015; Vasilopoulos & Petropoulou 2016). Time lags are caused by the arrival time differences of scattering photons with different light paths (Xu, McCray & Kelley 1986). Based on simple geometrical calculations, the time lag of a scattering photon relative to an un-scattered photon can be derived as

$$\Delta t(x,\theta,\ell) = \frac{\ell}{c}\left(\sqrt{\left(\frac{x}{\cos\theta}\right)^2 - 2x + 1} + \frac{x}{\cos\theta} - 1\right), \quad (7)$$

where c is the speed of light. Since dust scattering mainly happens at small angles, $\Delta t(x, \theta, \ell)$ can be simplified with small angle approximations:

$$\Delta t(x,\theta,\ell) \approx (1.21\,{\rm s})\,\frac{x}{1-x}\,\theta({\rm arcsec})^2\,\ell({\rm kpc}). \quad (8)$$

According to these equations, for a viewing angle of 2 arcsec to a dust grain at $x = 0.9$ from a source at $\ell = 8$ kpc, the lag is 350 s. These equations also show that time lag increases with increasing viewing angles. For a fixed viewing angle, the time lag increases as the scattering dust is located closer to the source. The lag scales linearly with the absolute source distance.

Downloaded from https://academic.oup.com/mnras/article/468/3/2532/3072846 by Biblioteca di Scienze tecnologiche user on 30 December 2020

1.2 Dust grain models

The modelling of the dust-scattering halo strongly depends on the dust grain model (e.g. Xiang et al. 2005; Valencic & Smith 2015). The classic dust grain model, proposed by Mathis, Rumpl & Nordsieck (1977) (hereafter MRN77 dust grain), assumes a power-law form for the size distribution of graphite and silicate grains with a size range of 0.005–0.25 μm. Later, a smaller size carbonaceous grain population (in the form of polycyclic aromatic hydrocarbon – PAH) was added to explain the infrared (IR) emission features and to reproduce the 2175Å hump in the ultraviolet extinction curve Li & Draine 2001; Weingartner & Draine 2001 – hereafter WD01, dust grains for different R_V (def. $A(V)/E(B-V)$) and carbon abundance; Draine 2003. Zubko, Dwek & Arendt (2004) (hereafter ZDA04) considered various forms of carbon in the ISM, different abundances and composite particles encompassing organic refractory material ($C_{25}H_{25}O_5N$), water ice (H_2O) and voids, and proposed 15 dust grain models that can all reproduce the $R_V = 3.1$ extinction curve. Moreover, Xiang et al. (2011) proposed a different dust grain model (XLNW) where the olivine grains in the BARE-GR-S dust grain model (BARE: without composite grains; GR: graphite; S: solar abundances) of ZDA04 is replaced with a new type of grain comprising a metallic iron core and a troilite/enstatite shell.

Due to the lack of knowledge about the dust grain composition and size distribution in different locations of the ISM, previous studies about the dust-scattering halo often adopted various dust grain models and compared the results. It was reported that the BARE-dust grains in ZDA04 were better than COMP-dust grains (with composite grains) in terms of fitting the halo around sources whose LOS has a short overlap with the Galactic plane (Valencic et al. 2009; Xiang et al. 2011; Valencic & Smith 2015). For the GC LOS, Fritz et al. (2011) measured the extinction curve within 1–19 μm and fitted various dust grain models to the IR extinction curve, and reported the necessity of adding composite dust grains containing H_2O to the pure carbonaceous and silicate grains. Therefore, the COMP-AC-S dust grain model (AC: amorphous carbon) of ZDA04 was proposed, for the first time, to be the best dust grain model for the GC LOS.

1.3 AX J1745.6−2901

The GC region is filled with intense and complex diffuse emission, so a bright X-ray source is required to produce a detectable bright dust-scattering halo that overwhelms the diffuse emission. Then the intrinsic halo profile can be extracted with enough signal-to-noise ratio (S/N) to study the dust properties along the LOS. AX J1745.6−2901 is an ideal source because it can be very bright in X-rays. It is a low-mass X-ray binary (LMXB) consisting of a neutron star and a K0V-type companion star (Ponti et al. 2015a). It was first discovered during *ASCA* observations of the GC in 1993 as an eclipsing transient (Kennea & Skinner 1996; Maeda et al. 1996). *Chandra* observations provided precise measurements of its coordinate (17:45:35.64, -29:01:33.90 with a 1σ coordinate error of 0.32 arcsec),[1] which is only 1.45 arcmin from Sgr A* (Heinke et al. 2009). Therefore, it has been intensely observed by many X-ray observatories such as *Chandra*, *XMM–Newton*, *Swift* and *Suzaku* during GC monitoring campaigns (Hyodo et al. 2009; Degenaar et al. 2012; Ponti et al. 2015b).

Previous observations revealed periodic eclipsing and irregular dipping in the light curve of AX J1745.6−2901, indicating a high inclination angle of this binary system (Maeda et al. 1996) with an orbital period of 30 063.74 ± 0.14 s and an eclipse duration of ∼1440 s (Hyodo et al. 2009). Analysing more than 20 yr of *XMM–Newton* and *ASCA* observations, Ponti et al. (2017a) measured a long-term decrease in the orbital period of $(4.03 \pm 0.32) \times 10^{-12} s/s$ as well as significant jitter.

AX J1745.6−2901 is one of the brightest X-ray transients within a few arcmin of Sgr A*(Degenaar et al. 2012; Ponti et al. 2015a). Its luminosity was observed to reach a few per cent Eddington luminosity assuming that the source is inside the GC region (i.e. within a few hundred pc from Sgr A*), which is within the typical luminosity range for 'atoll' sources (Gladstone, Done & Gierliński 2007). The $N_{\rm H,\,abs}$ towards AX J1745.6−2901 is measured to be $\sim 2.0 \times 10^{23}\,{\rm cm}^{-2}$ by Ponti et al. (2015a) from fitting the *XMM–Newton* spectra with the XSPEC PHABS absorption model and solar abundances of Anders & Grevesse (1989) (hereafter AG89). But Paizis et al. (2015) fitted the *Chandra* spectra with the TBABS model and ISM abundances of Wilms, Allen & McCray (2000) (hereafter WAM00), and reported $N_{\rm H,\,abs} = 3.4 \times 10^{23}\,{\rm cm}^{-2}$. The difference mainly arise from different assumptions about the abundances. In comparison, the $N_{\rm H,\,abs}$ measured from Sgr A*'s X-ray flares is $1.23 \times 10^{23}\,{\rm cm}^{-2}$ using the WABS model and Anders & Ebihara (1982) solar abundances (Porquet et al. 2008), or $1.5 \times 10^{23}\,{\rm cm}^{-2}$ using the TBNEW model and WAM00 ISM abundances (Nowak et al. 2012), which is also consistent with $1.6 \times 10^{23}\,{\rm cm}^{-2}$ measured most recently by Ponti et al. (2017b) using the same absorption model and abundances. These $N_{\rm H,\,abs}$ measurements are all significantly smaller than that of AX J1745.6−2901. Moreover, Degenaar & Wijnands (2009) reported the brightest X-ray burst from this source reaching a luminosity of $1.3 \times 10^{38}\,{\rm erg\,s}^{-1}$ for a GC distance of 8 kpc, approaching the Eddington luminosity of a typical neutron star (e.g. Kuulkers et al. 2003). Therefore, it can be inferred that AX J1745.6−2901 is likely located inside or behind the GC.

This paper presents a detailed analysis of the dust-scattering halo around AX J1745.6−2901. We organize this paper as follows. In Section 2, we describe the *Chandra* and *XMM–Newton* observations of AX J1745.6−2901 and data reduction, as well as the steps to extract the dust-scattering halo around AX J1745.6−2901. Section 3 describes the point spread function (PSF) of *Chandra* and *XMM–Newton*. Section 4 presents a detailed modelling of the dust-scattering halo in order to explore the properties of the dust grains along the LOS. The effect of the dust scattering on the observed spectra is studied in Section 5. Discussions about the dust properties towards AX J1745.6−2901 and more details about the halo profile are all included in Section 6. The final section summarizes our work and provides the main conclusions. Throughout this paper, we adopt a distance of 8 kpc to the GC (Reid et al. 2009; Genzel et al. 2010; Boehle et al. 2016), the uncertainty of which should not affect the results of this work.

[1] Degenaar & Wijnands (2009) report a similar *Chandra* position with a 1σ coordinate error of 0.6 arcsec. To improve the astrometric accuracy, we choose a long *Chandra* observation (ObsID:03665, 89.9 ks exposure time), where AX J1745.6−2901 is faint (so it is free from photon pile-up) but still have 285 counts for an accurate position measurement. We find three bright stars in the Tycho-2 catalogue detected in the soft X-ray band within the *Chandra* field of view (FoV), and use them to perform a high-precision astrometry correction, which then allows us to reduce the coordinate error by a factor of 2.

Downloaded from https://academic.oup.com/mnras/article/468/3/2532/3072846 by Biblioteca di Scienze tecnologiche user on 30 December 2020

Table 1. List of *XMM–Newton* and *Chandra* observations used for this paper. The list of observations during which AX J1745.6−2901 was in quiescence can be found in Appendix B. 'Exp' is the total exposure time and 'CL-Exp' is the good exposure time after subtracting the periods of background flares. $\theta_{\rm off}$ is the off-axis angle of AX J1745.6−2901. $r_{\rm pileup}$ is the inner circular radius of the PSF affected by photon pile-up (Section 2). 'PFW': primary full window mode. 'HETG': high energy transmission grating.

Chandra Obs-ID	Obs-Date	Target	ACIS (Grating)	Exp (ks)	CL-Exp (ks)	$\theta_{\rm off}$ (arcmin)	$r_{\rm pileup}$ (arcsec)
9169	2008-05-05	Sgr A*	ACIS-I (None)	27.6	27.6	1.45	2.0
9170	2008-05-06	Sgr A*	ACIS-I (None)	26.8	26.8	1.45	2.0
9171	2008-05-10	Sgr A*	ACIS-I (None)	27.7	27.7	1.45	2.1
9172	2008-05-11	Sgr A*	ACIS-I (None)	27.4	27.4	1.45	2.2
9174	2008-07-25	Sgr A*	ACIS-I (None)	28.8	28.8	1.45	2.0
9173	2008-07-26	Sgr A*	ACIS-I (None)	27.8	27.8	1.45	2.0
17857	2015-08-11	AX J1745-2901	ACIS-S (HETG)	117.2	111.1	0.00	2.4
XMM–Newton Obs-ID	Obs-Date	Target	pn-Filter	Exp (ks)	CL-Exp (ks)	$\theta_{\rm off}$ (arcmin)	$r_{\rm pileup}$ (arcsec)
0402430701	2007-03-30	Sgr A*	PFW-Medium	34.2	21.3	1.46	20
0402430301	2007-04-01	Sgr A*	PFW-Medium	105.4	56.1	1.46	20
0402430401	2007-04-03	Sgr A*	PFW-Medium	105.8	38.1	1.46	20
0505670101	2008-03-23	Sgr A*	PFW-Medium	105.7	64.5	1.68	20
0724210201	2013-08-30	Sgr A*	PFW-Medium	58.5	53.4	1.45	20
0700980101	2013-09-10	Sgr A*	PFW-Medium	38.7	35.8	1.46	20
0724210501	2013-09-22	Sgr A*	PFW-Medium	43.9	32.2	1.45	20
0743630801	2015-04-01	Sgr A*	PFW-Medium	27.0	23.4	1.45	20

2 OBSERVATION AND DATA REDUCTION

AX J1745.6−2901 is one of the brightest transients within a few arcmin from Sgr A*. Being so close, it is in the FoV of many observations targeting Sgr A*. In this work, we used archival and new *Chandra* and *XMM–Newton* observations. *Chandra* has a high spatial resolution and small PSF, which can produce high-resolution halo radial profiles, while *XMM–Newton* provides a large effective area and FoV, which leads to a significant detection of the dust-scattering halo up to 10 arcmin. Therefore, combining the data from these two satellites is ideal to study the halo profile.

2.1 *Chandra* observations

The *Chandra* data website was used to search for observations of AX J1745.6−2901.[2] We selected observations where AX J1745.6−2901 was observed at ≤3 arcmin off-axis angle[3] because of significant PSF degradation at larger off-axis angles. Among these observations, we chose those where AX J1745.6−2901 was bright enough to show a clear halo above 2 keV ($L_{2\text{–}4\,\rm keV} \geq 10^{-12}$ erg cm^{-2} s^{-1}). Then we dropped observations with short exposures ($\lesssim$5 ks), as these observations were too short to constrain the halo profile. Our selection resulted in six ACIS-I observations targeting Sgr A* and one recent ACIS-S observation targeting AX J1745.6−2901 (Table 1).

In order to measure the detector background and diffuse emission underneath AX J1745.6−2901 , we made use of observations where AX J1745.6−2901 was at ≤3 arcmin off-axis angle but was in the quiescent state. To ensure that the non-detection of AX J1745.6−2901 was due to its intrinsic weakness rather than the short exposure time, we chose observations with more than 15 ks exposure and found 17 such observations in the ACIS-I mode (with 713.3 ks clean exposure in total) and 12 observations in the ACIS-S mode (with 702.7 ks clean exposure in total) (Table B1). The long accumulated exposure time allows an accurate determination of both the detector background and the diffuse emission in this region. Moreover, we checked that AX J1745.6−2901 was located in the same type of CCD chip, i.e. front-illuminated chip in ACIS-I and back-illuminated chip S3 in ACIS-S. This is to ensure the consistency of the detector background among all observations in ACIS-I and ACIS-S, separately.

The *Chandra* software CIAO (v4.8.1) and Chandra Calibration Database (CALDB, v4.7.2) were used to analyse all the *Chandra* observations following the standard data reduction steps (see e.g. Clavel et al. 2013 for detailed descriptions). First, the CHANDRA_REPRO script was used to reprocess all the Advanced CCD Imaging Spectrometer (ACIS) data. To ensure the astrometry consistency among all the observations, we followed the standard thread to perform the astrometry correction by taking ObsID:14468 (146 ks exposure time) as the reference observation. For every observation, we used the WAVDETECT script to perform the point source detection and all the point sources were excluded before extracting the background light curve, which was then used as the input for the DEFLARE script to remove the background flares from the event file. AX J1745.6−2901 was piled up in all the selected observations, so we used the PILEUP_MAP script in CIAO (v4.8.1) to estimate the size of the 1 per cent pile-up region around AX J1745.6−2901 (Table 1). All data within this pile-up radius were removed from our study. Furthermore, we excluded the data when AX J1745.6−2901 was in the eclipsing phase (detected in five observations, ObsID: 9169, 9170, 9173, 9174 and 17857) and 300 s after the eclipse egress time. This is because the halo profile was varying due to a delayed response to the eclipsed signal, which needs to be studied independently (Jin et al., in preparation).

We used the MERGE_OBS script and REPROJECT_IMAGE_GRID script in the *Chandra* software to create images and exposure maps

[2] http://cda.harvard.edu/chaser

[3] The angle between the High-Resolution Mirror Assembly (HRMA) optical axis and the source position.

Downloaded from https://academic.oup.com/mnras/article/468/3/2532/3072846 by Biblioteca di Scienze tecnologiche user on 30 December 2020

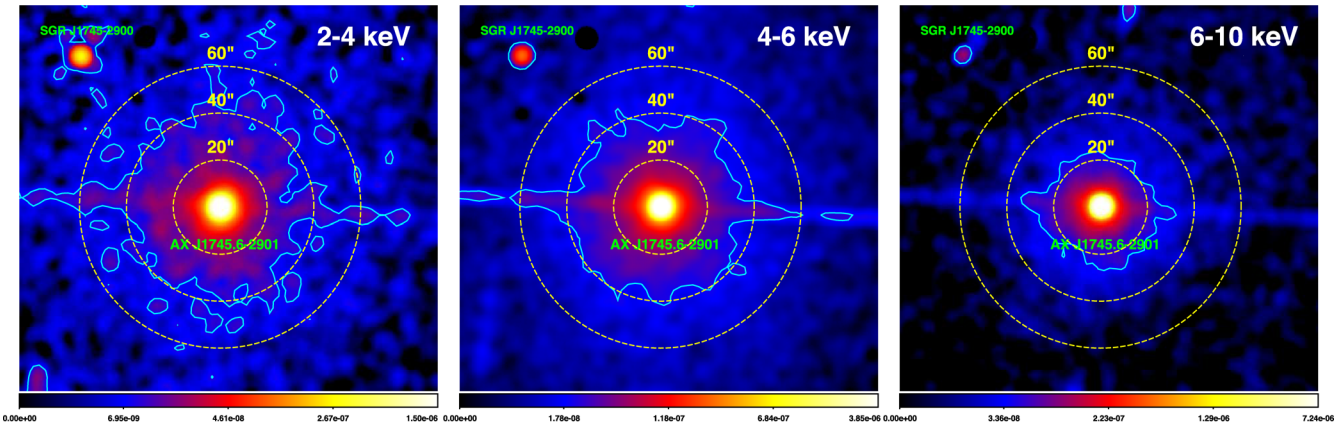


Figure 2. *Chandra* ACIS-S (ObsID:17857) flux images of AX J1745.6−2901 in the 2–4, 4–6 and 6–10 keV bands, showing the shrink of the dust-scattering halo towards higher energies. The background based on 12 ACIS-S observations with AX J1745.6−2901 in quiescence has been subtracted (see Section 2). In every panel, the cyan contour indicates the location where the surface brightness is only 0.4 per cent of the value at 2.5 arcsec from the core (inside which more than 1 per cent pile-up is expected). The dashed yellow circles indicate regions with 20-, 40- and 60-arcsec radius centred on AX J1745.6−2901. Note that the horizontal structure across AX J1745.6−2901 is due to the readout streak.

(including the vignetting effect), re-project the images and combine images from all observations. The DMIMGCALC script was used to perform background subtraction. Fig. 2 shows the final flux images of AX J1745.6−2901 in 2–4, 4–6 and 6–10 keV bands from the ACIS-S observation (ObsID: 17857). It is clear that AX J1745.6−2901 appears much more extended than a point-like source, and the extension has a clear energy dependence, consistent with the prediction of the dust-scattering theory.

To extract the radial profile of AX J1745.6−2901, we first excluded all other point sources including transients in every observations, then an elliptical region of 2×6 arcmin^2 was used to exclude the region around Sgr A* where the diffuse emission is strongest (e.g. Heard & Warwick 2013a,b; Ponti et al. 2015b). All artificial features such as the readout streak and the high-energy transmission grating (HETG) arms (in ACIS-S observations) were also masked out by employing box regions of 7-arcsec wide from the edge of the FoV down to 2 arcsec from AX J1745.6−2901. We defined a set of annulus regions, and used the FUNTOOLS in *ds9* to extract the photon counts and exposure in every annulus region from the image and exposure map of every observation.[4] The combined radial profile was obtained by adding counts from all observations and dividing it by the total exposure time in every annulus region. The Poisson counting errors are small because of the accumulated number of counts from all the observations, but there are additional small dispersions in the shape of radial profiles from different observations due to the fluctuation of residual background contamination from, for example, the extended PSF wing of bright sources and diffuse emission in the FoV. Therefore, we used the MPFITEXY routine (Markwardt 2009; Williams, Bureau & Cappellari 2010) to calculate error bars for the combined radial profile, which takes into account both the Poisson error and the small dispersion between different observations (see Tremaine et al. 2002 for the statistical method).

The above procedure was repeated to create the radial profile of AX J1745.6−2901 as well as the radial profile of the underlying diffuse emission and detector background when AX J1745.6−2901 was in quiescence (Fig. 3a, also see Fig. A1 for the energy dependence of the radial profile). The intrinsic radial profile of AX J1745.6−2901 was derived by subtracting the combined radial profile observed when AX J1745.6−2901 was in quiescence from the one when AX J1745.6−2901 was bright, with the standard error propagations. Note that we did not combine the radial profiles from ACIS-I and ACIS-S observations, because the ACIS-S observation was in the sub-array mode. AX J1745.6−2901 was weakly detected in the combined background radial profile within 2 arcsec due to the enhanced S/N. We also repeated the above procedures to extract the mean radial profile of AX J1745.6−2901 during its eclipsing phase (Fig. 3a, red points), which allows us to observe the shape of the dust-scattering halo without the PSF of AX J1745.6−2901 itself. However, the light curve of AX J1745.6−2901 in Ponti et al. (2017a) shows that the halo is variable during the eclipsing phase due to the time-lag effect (see Section 1.1.2), so in this work, we do not model the halo profile in the eclipsing phase.

[4] Also see http://cxc.harvard.edu/ciao/threads/radial_profile

2.2 *XMM–Newton* observations

We used the *XMM–Newton* Science Archive to search for *XMM–Newton* (Jansen et al. 2001) observations of AX J1745.6−2901 with similar selection criteria as for the *Chandra* observations. We found nine observations where AX J1745.6−2901 was observed at $\leq$3 arcmin off-axis angle where the PSF was not degraded significantly, and the source was bright enough for a significant halo detection above 2 keV ($L_{2-4\,\mathrm{keV}} \geq 10^{-11}\,\mathrm{erg\,cm^{-2}\,s^{-1}}$). All these observations were in the same mode and targeted Sgr A* so that AX J1745.6−2901 was at the same off-axis angle. In order to determine the underlying diffuse emission and detector background, we selected another 14 observations targeting Sgr A* with $\gtrsim$15 ks exposure time but with no detection of AX J1745.6−2901 (so it was in quiescence). The accumulated exposure time is 358.3 ks, which can ensure an accurate measurement of the diffuse emission and detector background.

For each of these observations, we used the *XMM–Newton* Science Analysis System (SAS v15.0.0) to process the data and applied the most recent calibrations. We only focused on the EPIC-pn data, as pn provides the highest count rate among all three EPIC cameras. The EPCHAIN task was used to reprocess the data. Then we excluded all high background periods detected from the 7–15 keV background light curve, and followed the method in Urban et al. (2011) (also see Leccardi & Molendi 2008) to check and ensure

Downloaded from https://academic.oup.com/mnras/article/468/3/2532/3072846 by Biblioteca di Scienze tecnologiche user on 30 December 2020

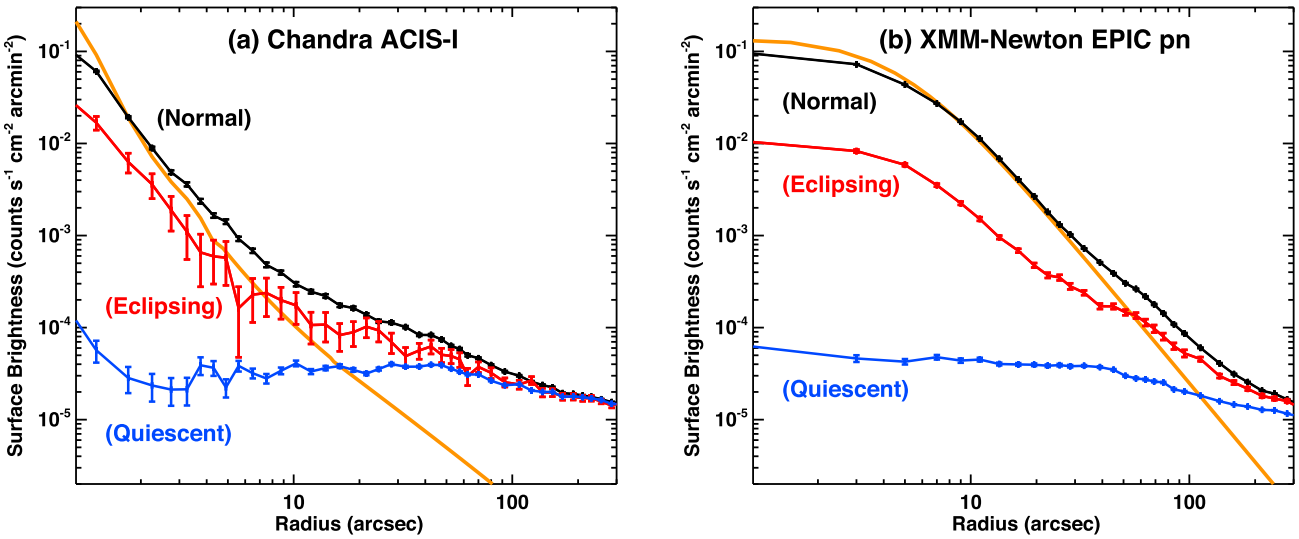


Figure 3. Radial profile of AX J1745.6−2901 in the normal (black) and eclipsing phases (red) in the 4–6 keV band. Panel (a) shows the combined radial profile from six *Chandra* ACIS-I observations in Table 1. The quiescent profile (blue) is based on a combination of 17 *Chandra* ACIS-I observations where AX J1745.6−2901 was in quiescent. The slight rising of the radial profile within 2 arcsec is due to the weak emission from AX J1745.6−2901 when several observations were combined. Panel (b) shows the combined radial profile from eight *XMM–Newton* observations in Table 1. The emission inside the eclipsing phase comes from the dust scattering. In both panels, the solid orange profile shows the instrumental PSF at 5 keV. The difference between the halo radial profiles of *Chandra* and *XMM–Newton* is caused by their different PSFs.

no significant soft proton residuals. We excluded one observation of AX J1745.6−2901 (ObsID: 0504940201), as the clean exposure time was only 6 ks. The remaining eight observations of AX J1745.6−2901 are listed in Table 1. The 14 observations that caught AX J1745.6−2901 in quiescence are listed in Table B1, with a total of 332.1 ks clean exposure time.

We used the EPATPLOT task to determine the pile-up region, and excluded data within 20 arcsec of AX J1745.6−2901 to safey avoid the pile-up effect. We double checked this radius by plotting in the radial dependence the ratios of single events and double events in all events for the observation (OBSID: 0743630801) where AX J1745.6−2901 had the highest flux (see Costantini, Freyberg & Predehl 2005). For the observed spectrum of AX J1745.6−2901, the pile-up effect is most obvious above 7 keV, and so we used events within 7–10 keV to perform this test. Fig. 4 shows that within 20 arcsec, the pile-up effect causes single event's ratio to be lower than expectation, and double event's ratio to be higher than expectation.

For every observation, the 2–10 keV light curve of AX J1745.6−2901 was extracted with the EVSELECT task. The light curve was used to search for eclipsing periods and the latter were excluded from the event file. We also carefully excluded some dipping periods. Then we used the Extended Source Analysis Software (SAS; Snowden & Kuntz 2011) in SAS (v15.0.0) to create and process images from the event file. We performed point source detection using the CHEESE task. Then the PN_SPECTRA task was used to create the normal and Out-of-Time (OoT) processing images and exposure maps (including the vignetting effect). The OoT image was multiplied by 0.063 and subtracted from the normal image using the FARITH task (FTOOLS v6.19). The PN_BACK task was used to create the particle background image and then subtracted this from the normal image.

All point sources except AX J1745.6−2901 were excluded in every observation before extracting the radial profile. An elliptical region of 12×16 arcmin^2 was used to exclude the strong diffuse emission around Sgr A*. We note that there were still residual

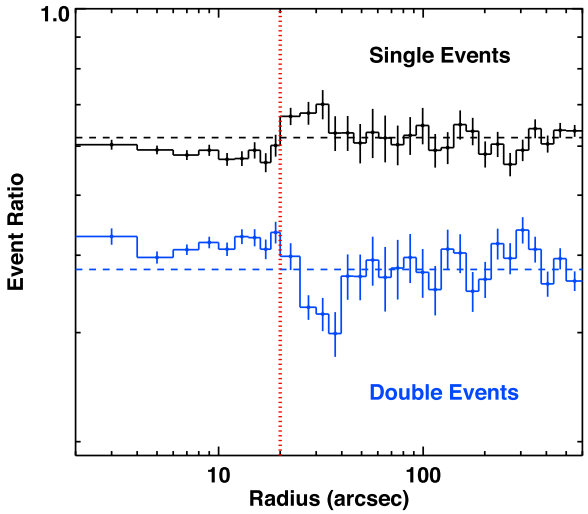


Figure 4. Radius dependence of the ratio between single events and all events (black), and between double events and all events (blue) for 7–10 keV in *XMM–Newton* (OBSID: 0743630801). The two horizontal dashed lines indicate the expectation of no pile-up effect. The vertical red dotted line indicates 20-arcsec radius within which the pile-up effect is seen.

OoT features in the final images of some observations, which was because AX J1745.6−2901 was piled up so that the correction was not accurate. Therefore, we visually checked all images and, when necessary, we used a rectangular region to mask out the OoT residual from the CCD edge down to 20 arcsec from AX J1745.6−2901. We chose the width of the rectangle up to 250 arcsec depending on the strength of the OoT residual feature. Some weak features near the edge of FoV due to stray light were also visually masked out. The exposure map created by the PN_BACK task was not multiplied by the effective area, so we used the SAS task PSFGEN to produce the unvignetted ancillary response file, from which we obtained the

Downloaded from https://academic.oup.com/mnras/article/468/3/2532/3072846 by Biblioteca di Scienze tecnologiche user on 30 December 2020

spectral shape-weighted effective area in every energy band. Finally, we obtain the combined radial profiles from all the observations and performed background subtraction using the same method as for *Chandra* (see Section 2.1 and Fig. 3b).

3 PSF OF *Chandra* AND *XMM–Newton*

The image of AX J1745.6−2901 consists of a central point source plus a dust-scattering halo, convolved with a two-dimensional (2D) instrumental PSF. This 2D convolution can significantly smooth the halo profile especially when the PSF is broad such as in *XMM–Newton*.

3.1 PSF of *Chandra* ACIS

The on-axis half-energy width of the PSF in the *Chandra* HRMA/ACIS is 0.4–0.7 arcsec within 0.3–10 keV (*Chandra* Proposers' Observatory Guide v18.0[5]), indicating that the halo profile detected by *Chandra* ACIS is heavily smeared by the PSF convolution (Smith, Edgar & Shafer 2002; Smith 2008). Therefore, an accurate PSF is mainly required to disentangle the point source from the dust-scattering halo. We used the web-based CHART software to perform the ray-trace simulation that takes parameters directly from real observations (ObsID:09174 for ACIS-I and ObsID:17857 for ACIS-S). The simulation was done for 50 iterations in order to obtain enough counts to extract a high S/N PSF.[6] Then the MARX (v5.3) software and DMMERGE script were used to create a combined pseudo-event file from all the 50 iterations. Finally, a high S/N PSF radial profile was extracted from the combined event file. This procedure was repeated for ACIS-I and ACIS-S at 3.3, 5.0 and 7.0 keV separately because AX J1745.6−2901 was at slightly different off-axis angles during these two observation modes. Note that in the simulations for ACIS-S, there was no typical 'X' pattern from the HETG arms, thus the simulated PSF profile is not affected by the gratings.

Meanwhile, Gaetz (2010) performed a detailed analysis of the PSF wing of HRMA using a deep calibration observation of the LMXB Her X-1 (ObsID: 3662), which is bright and has low $N_{\rm H,\,sca}$ in the LOS. This observation was also used in some other works to measure the PSF profile (e.g. Smith et al. 2002; Xiang, Lee & Nowak 2007; Xiang et al. 2011). Because Her X-1 was heavily piled up in the PSF core, we only used the best-fitting King profile in Gaetz (2010) to produce the PSF from 10 to 500 arcsec. Her X-1 was at a 0.75 arcmin off-axis angle during this observation, while AX J1745.6−2901 was on-axis in the ACIS-S mode and at 1.45 arcmin off-axis in the ACIS-I mode, but the small difference of the off-axis angle should not affect the PSF wing significantly (see the *Chandra* website[7] and Gaetz 2010).

Since the PSF from the CHART simulation for $E \geq 2$ keV may underpredict the flux in the PSF wing, 2 while the PSF from Gaetz (2010) was affected by severe pile-up within 10 arcsec, we decided to use the core of the CHART PSF and the wing of the Gaetz (2010) PSF by matching them within 10–15 arcsec, so that an accurate PSF profile was derived. This final PSF profile was renormalized and adopted in our halo profile modelling.

[5] http://cxc.harvard.edu/proposer/POG/html/chap6.html#tth_sEc6.6
[6] http://cxc.harvard.edu/ciao/PSFs/chart2/runchart.html
[7] http://cxc.harvard.edu/ciao/PSFs/chart2/caveats.html

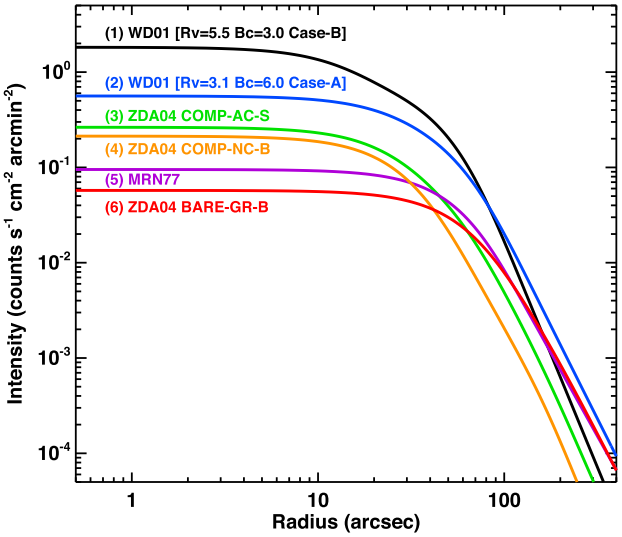


Figure 5. Radial profile comparison for some representative dust grain models. These radial profile models are for a source at 8.15 kpc with a flux of unity and $E = 5$ keV. The light passes through a single smoothly distributed dust layer between 2.5 and 3.5 kpc with a total $N_{\rm H,\,sca} = 1.5 \times 10^{23}$ cm^{-2}. No instrumental PSF was convolved. These radial profiles reveal the typical halo shape diversity among the dust grain models in MRN77, ZDA04 and WD01.

3.2 PSF of *XMM–Newton* EPIC-pn

The on-axis half energy width of EPIC-pn is 16.6 arcsec (*XMM–Newton* Users Handbook[8]), implying a much bigger impact on the halo profile than in *Chandra*. Ghizzardi (2002) studied 110 *XMM–Newton* observations to calibrate the EPIC-pn PSF and provided equations (based on the best-fitting King profile) to calculate the one-dimensional (1D) PSF profile (also see Costantini et al. 2005). Meanwhile, the 1D and 2D PSF profiles were modelled separately with a 1D King profile and a 2D ELLBETA model by the *XMM–Newton* calibration team (Read et al. 2011), with the best-fitting parameters given in the latest current calibration files (CCF). However, it was noticed that the 2D ELLBETA model requires further calibration in the PSF wing (Schartel, private communication), while the CCF files only provide 1D PSF parameters for a discrete set of off-axis angles and energies, so we decided to adopt the Ghizzardi (2002) PSF that should be accurate enough for our study. Note that the off-axis angle of AX J1745.6−2901 is 1.454–1.678 arcmin in all the EPIC-pn observations, and the PSF changes very little within these small off-axis angles.

4 MODELLING THE DUST-SCATTERING HALO OF AX J1745.6−2901

4.1 Radial profile fitting of the dust-scattering halo

The shape of the dust-scattering halo depends on the dust grain model (see Section 1.2). In Fig. 5, we compare the halo profiles using some representative dust grain models, including the classic MRN77 dust grain model, two dust grain models from WD01 with $[R_V = 3.1, Bc = 6.0, Case - A]$ (adopted by Valencic & Smith 2015 as the standard WD01 dust grain model) and $[R_V = 5.5, Bc = 3.0, Case - B]$ (highest intensity in the halo

[8] http://www.cosmos.esa.int/web/xmm-newton/documentation

Downloaded from https://academic.oup.com/mnras/article/468/3/2532/3072846 by Biblioteca di Scienze tecnologiche user on 30 December 2020

core), where Bc ($\times 10^5$) is the carbon abundance per hydrogen nucleus, and three ZDA04 dust grain models. In this paper, we tried all dust grain models in MRN77, WD01, ZDA04 and XLNW to do the halo profile modelling and compared the results.

A reasonable dust-scattering model should reproduce not only the halo radial profile at a specific energy, but also the energy dependence of the halo. Besides, the halo profiles from *Chandra* and *XMM–Newton* should contain the same intrinsic halo shape except for the different instrumental PSF. Therefore, we decided to fit the halo profiles from *Chandra* ACIS-I and *XMM–Newton* in the 2–4, 4–6 and 6–10 keV bands, simultaneously, i.e. six radial profiles in total (see Fig. 9). The dust-scattering calculation is computationally intensive (Corrales & Paerels 2015; Smith et al. 2016). In order to increase the computing efficiency, we calculated the spectral weighted effective energy within the 2–4, 4–6 and 6–10 keV bands as 3.3, 5.0 and 7.0 keV and fixed the photon energy at these values in the model. This should not affect the accuracy because the halo shape is not sensitive to a small change of the effective energy. Assuming a rotational symmetry, we performed 2D convolution for the instrumental PSF in order to fit the halo profile observed by various instruments. All the fittings were performed with the SHERPA fitting engine provided in the CIAO (v4.8.2) software.[9]

4.1.1 One dust-layer model

First, we assumed a point source and one foreground dust layer of smooth distribution (as shown in Fig. 1). The lower and upper boundary of the dust layer and the $N_{\rm H,\,sca}$ were all free parameters. The incident flux to the dust layer was linked to the flux of the point source, which was also a free parameter because the fraction of scattering flux in the total observed flux was unknown. Only single scattering was considered (see Section 4.2 for the discussion of multiple scattering). The absolute distance of AX J1745.6−2901 does not affect the halo profile fitting because all distances in the model are fractional. Fig. 6 shows an example of the one-layer model fit to the 4–6 keV radial profile of AX J1745.6−2901 observed by *Chandra* ACIS-I, using the COMP-AC-S dust grain model. The best-fitting $\chi^2 = 1329$ for 178 degrees of freedom (dof) for all six radial profiles. The fitting also required the dust layer to extend from Earth to the source with $N_{\rm H,\,sca} = 1.7 \times 10^{23}$ cm^{-2}. It is clear that this model is too simple to reproduce the halo profile around AX J1745.6−2901. We tried other dust grain models but none could produce a reasonably good fit with reduced $\chi^2_\nu < 2$. The residuals in Fig. 6 clearly indicate that the curvature of the radial profile is more complex than the dust-scattering halo from one smooth dust layer regardless of the dust grain model used.

4.1.2 Two dust layers without wing

Then we adopted a two-layer model, i.e. layer-1 + layer-2. Fig. 7 shows the set-up and free parameters of the two dust layers, including the $N_{\rm H,\,sca}$, lower and upper boundaries of each layer. Layer-1 was closer to AX J1745.6−2901 and layer-2 was closer to Earth, and so the halo from layer-2 was more extended than that from layer-1. The parameters of these two layers were independent of each other. As a first-order consideration, we assumed the same dust grain model for the two layers. This two-layer model improved the halo fitting significantly. For example, we found $\chi^2 = 664$ for 175 dof in the case of COMP-AC-S dust grain model. Fig. 8 shows

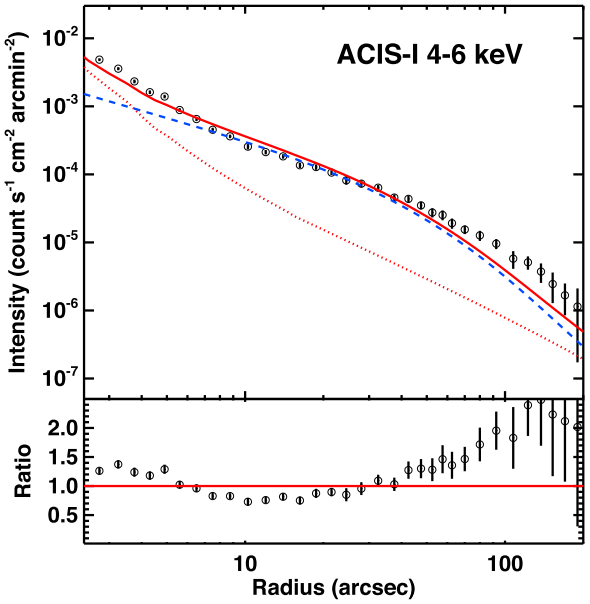


Figure 6. Radial profile observed by *Chandra* ACIS-I in the 4–6 keV band. The model comprises the ACIS-I PSF (red dotted curve) and a single dust layer smoothly distributed from Earth to AX J1745.6−2901(blue dashed curve), which used the COMP-AC-S dust grain model. The lower panel shows the residuals.

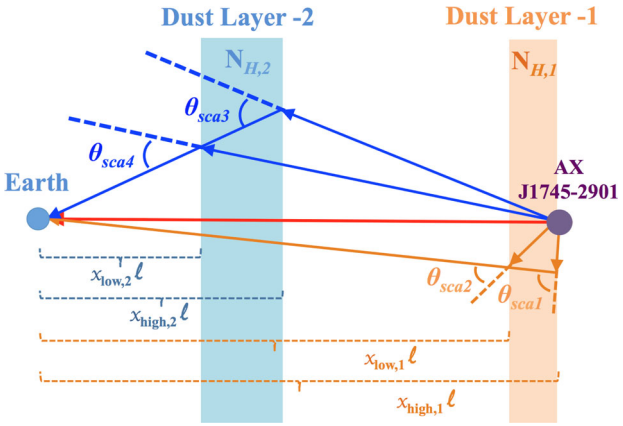


Figure 7. The two dust-layer scenario for the radial profile fitting in Fig. 9. $x_{\rm low,\,1,\,2}$ and $x_{\rm high,\,1,\,2}$ are the fractional distances of the two dust layers from Earth. $N_{\rm H,\,1}$ and $N_{\rm H,\,2}$ are the $N_{\rm H,\,sca}$ in layer-1 and layer-2, separately. ℓ is the absolute distance of AX J1745.6−2901 from Earth. $\theta_{\rm sca1,\,2}$ and $\theta_{\rm sca3,\,4}$ show the change of dust-scattering angle at a specific viewing angle within the two dust layers.

that this two-layer model cannot fit the halo wing ≥200 arcsec observed by *XMM–Newton*. The discrepancy between the wing and the best-fitting model increases towards large radii up to a factor of 6 at 600 arcsec. The total flux in the detected halo wing (200–600 arcsec) is a factor of 6.0 ± 1.0 higher than in the model. We emphasize that the fractional distance of layer-2 in Fig. 8 (blue dashed curve) has already pegged at 0 with the fractional width reaching the lower limit of 0.01, indicating that this wing component cannot be solely explained by the distance of the layer.[10] We find that this wing component is related to the X-ray emission from

[9] http://cxc.cfa.harvard.edu/ciao

[10] We chose 0.01 to avoid numerical problem in the halo calculation. Changing it to an even smaller value causes negligible difference to the halo profile.

Downloaded from https://academic.oup.com/mnras/article/468/3/2532/3072846 by Biblioteca di Scienze tecnologiche user on 30 December 2020

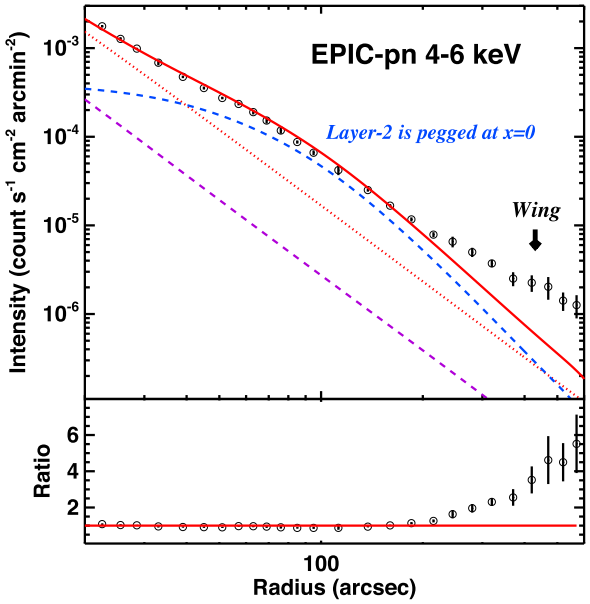


Figure 8. Radial profile observed by *XMM–Newton* EPIC-pn in the 4–6 keV band, overplotted with the EPIC-pn PSF (red dotted curve), dust layer-1 (magenta dashed curve), layer-2 whose fractional distance is pegged at 0 and fractional width pegged at the lower limit of 0.01 (blue dashed curve), and the total model (red solid curve). A significant excess flux exists outside 200 arcsec, which cannot be fitted by any dust model (black arrow).

AX J1745.6−2901 and rises from some dust grains with relatively small sizes (see Section 6.3), while scattering from large dust grains still dominates at small radii.

4.1.3 Two dust layers with wing

Because of the halo wing component detected, we restricted our fitting to the radial profile less than 300 arcsec and added a free constant parameter to the model to account for the wing above 200 arcsec. Since this wing component should exist in both *Chandra* and *XMM–Newton* observations, we assumed that it had the same scaling factor to the source flux in both instruments. Therefore, the final two-layer model was layer-1 + layer-2 + wing.

Based on this new two-layer model, we fitted the halo profile with various dust grain models. Fig. 9 shows the halo fitting for the COMP-AC-S dust grain model. 18 out of 19 dust grain models produce $\chi^2_v < 2$, indicating a reasonably good fit. The best $\chi^2_v = 1.29$ was found by the BARE-GR-B dust grain model (Table 2). The best-fitting parameters and their statistical errors are listed in Tables 2 and 3. It is clear that the statistical errors are much smaller than the dispersion of best-fitting values among all the dust grain models, indicating significant systematic uncertainty due to the assumptions made in the dust grain model. Other systematics include the assumptions about the uniform dust distribution inside every layer, the same dust grain model for all the foreground dust, Gaussian approximation for the form factor and calibration systematics especially in the PSF wing.

Among all the 19 dust grain models, the highest $N_{\rm H,\,sca} = (29.7 \pm 1.3) \times 10^{22}$ cm^{-2} was found for the COMP-AC-B dust grain model, while the lowest $N_{\rm H,\,sca} = (5.0 \pm 0.2) \times 10^{22}$ cm^{-2} was found for the WD01-B dust grain model. This large $N_{\rm H,\,sca}$ dispersion was also found in previous works (e.g. Smith et al. 2002; Valencic & Smith 2008; Valencic et al. 2009; Xiang et al. 2011), which is mainly due to different assumptions about the dust-to-gas ratio, abundances and size distribution made in different dust grain models. However, the mean best-fitting $N_{\rm H,\,sca} = 16.9 \times 10^{22}$ cm^{-2} and the COMP-AC-S best-fitting $N_{\rm H,\,sca} = 19.2 \times 10^{22}$ cm^{-2} are still roughly consistent with $N_{\rm H,\,abs} \sim 2.0 \times 10^{23}$ cm^{-2} using the AG89 solar abundances (Ponti et al. 2015a).

For all dust grain models, the fitting requires dust layer-1 to be close to AX J1745.6−2901. Depending on the dust grain model used, the fractional distance of layer-1 is $\lesssim$0.1 from the source and containing (19–34) per cent of the total dust along the LOS. Layer-2 is more extended and contains (66–81) per cent of the intervening dust, with its lower boundary always pegged at 0, indicating that part of this layer is very close to Earth. From Table 2, we see that the upper boundary of layer-2 ($x_{\rm high,\,2}$) also depends on the dust grain model, ranging from 0.01 to 0.90. The lowest values are found in the COMP-NC-B ($x_{\rm high,\,2} = 0.01$) and COMP-NC-GF ($x_{\rm high,\,2} = 0.11$) dust grain models, but their χ^2 are also the largest. The highest value is found in the BARE-GR-B model ($x_{\rm high,\,2} = 0.90$). We notice that the boundary of the two layers mainly depends on the size distribution of dust grains in each model. A higher fraction of small dust grains will produce a more extended halo profile, and so $x_{\rm high,\,2}$ ($x_{\rm low,\,1}$) will increase (decrease) to enhance the halo intensity at small radii in order to fit the observed halo profile. The mean $x_{\rm high,\,2}$ is 0.64, which is about half way towards AX J1745.6−2901. The separation between these two layers is quite significant compared to the statistical error, although the value ranges from 0.09 to 0.88 among all the dust grain models (Table 3). Adding more dust layers can improve the fitting statistics but also introduce more parameter degeneracies. To better resolve these two major dust layers, it is necessary to consider the timing properties of the halo due to the variability of AX J1745.6−2901 (e.g. the eclipsing signal), which will be presented in a separate work (Jin et al., in preparation).

4.2 Optical depth and multiple scattering

Although our two-layer single scattering model can provide a reasonably good fit to the halo profile of AX J1745.6−2901 in all three energy bands, it is still necessary to check if multiple scattering is important. The inclusion of higher order scattering will produce a brighter and more extended halo than single scattering (Mathis & Lee 1991). Multiple scattering starts to dominate when the scattering optical depth ($\tau_{\rm sca}$) is significantly bigger than unity (e.g. Xiang et al. 2007; Mathis & Lee 1991). Since AX J1745.6−2901 is an eclipsing source, the total flux and halo flux can be measured directly from inside and outside the eclipsing phase, then $\tau_{\rm sca}$ can be calculated using equation (6).

In order to measure the flux accurately, we chose a different *XMM–Newton* observation (ObsID: 0723410301) where AX J1745.6−2901 was not piled up. The same data reduction procedures were applied to this observation. Source light curves were extracted from a circular region of 200 arcsec to include the dust-scattering halo in the 2–4, 4–6 and 6–10 keV bands. The remaining halo flux outside 200 arcsec should be negligible (see Fig. 9). From background-subtracted light curves, $F_{\rm sca}/F_{\rm obs}$ was found to be 0.57, 0.32 and 0.16 for the three energy bands, implying $\tau_{\rm sca} = 0.84$, 0.39 and 0.17. We also calculated $\tau_{\rm sca}$ from every best-fitting two-layer model, which are consistently less than 1 (Table 3). Similar results can be found using common relations between $\tau_{\rm sca}$, $N_{\rm H,\,abs}$ and the V-band extinction A_V (see Section 6.2). These scattering optical depths indicate that single scattering should dominate in the case of AX J1745.6−2901. As a further check, we followed the equations in Mathis & Lee (1991) and Xiang et al. (2007) to calculate the halo profile from double scattering using the best-fitting COMP-AC-S

Downloaded from https://academic.oup.com/mnras/article/468/3/2532/3072846 by Biblioteca di Scienze tecnologiche user on 30 December 2020

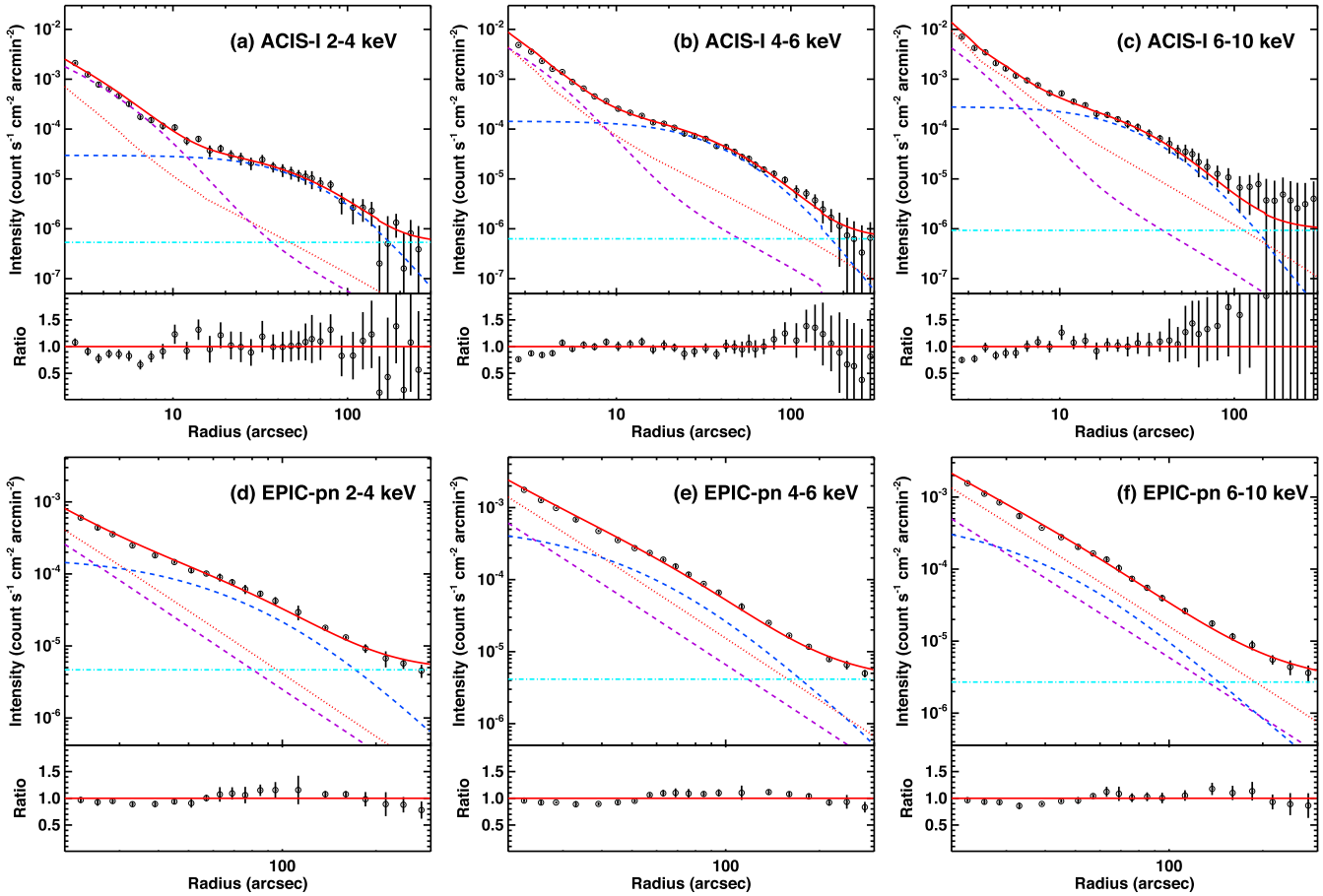


Figure 9. The radial profile fitting for *Chandra* ACIS and *XMM–Newton* EPIC pn in the 2–4, 4–6 and 6–10 keV bands using two dust layers with the COMP-AC-S dust grain model (ZDA04). The background is already subtracted (see Section 2.1). The red solid curve shows the total model. The red dotted curve shows the instrumental PSF. The two dashed curves show the dust scattering from the two dust layers (magenta: layer-1; blue: layer-2). The cyan line is a flat component to account for the halo wing dominating outside ∼200 arcsec, which cannot be reproduced directly by any dust grain model (see Section 6.3). The best-fitting parameters can be found in Table 2. The radial profiles before background subtraction can be found in Fig. A1.

two-layer model. Fig. 10 shows that the intensity of the double-scattering component is indeed dominated by the single-scattering component. Therefore, we conclude that it is sufficient to consider only single scattering in this work.

5 IMPACT OF THE DUST SCATTERING FOR SOURCE SPECTRA

5.1 Extraction region dependence of the observed spectrum

X-ray photons passing through the ISM are exposed to both photoelectric absorption and scattering by dust grains (Draine 2003; Ueda et al. 2010). Recent studies on simulated *Chandra* spectra show that the $N_{\rm H,\,abs}$ can be overestimated by 25 per cent if the dust-scattering opacity is not considered in the spectral fitting (Corrales et al. 2016). Assuming a similar dust-to-gas ratio, the spectral effect of the dust-scattering opacity becomes more significant for sources with higher $N_{\rm H,\,abs}$, such as many sources in the GC.

Dust along the LOS can scatter X-ray photons out of the LOS, which are partially compensated by the photons scattered into the LOS and are subsequently included in the spectral extraction region (see fig. 1 in Smith et al. 2016). If an infinite spectral extraction region is adopted, the loss of LOS photons will be fully compensated by the extra photons from the entire dust-scattering halo, thereby leaving no dust-scattering opacity in the observed spectrum. In reality, the spectral extraction region has a limited size. Besides, a small region of the PSF core is sometimes excised in order to avoid the photon pile-up. Therefore, the effective dust-scattering opacity is often non-zero and so affects the observed spectrum.

Based on our halo profile modelling, we can investigate this spectral effect for AX J1745.6−2901. We extracted *XMM–Newton* pn spectra from an observation (ObsID:0724210201) with two annulus regions (i.e. 15–40 and 20–80 arcsec) and applied the PSF correction using SAS task ARFGEN. Background spectra were extracted from an observation (ObsID:0658600201) where AX J1745.6−2901 was in quiescence. Fig. 11 shows that the two source spectra (background-subtracted) differ significantly from each other in terms of both spectral shape and flux. The spectral difference increases towards soft X-rays, which is consistent with the fact that the effect of dust scattering is stronger for lower energy photons. We note that there could also be spectral discrepancies due to an annulus extraction region for point-like sources because of the PSF calibration issue.[11] but this type of spectral discrepancy is mainly above 4 keV, with

[11] http://www.cosmos.esa.int/web/xmm-newton/sas-watchout-epic-spectra-annular-sources

Downloaded from https://academic.oup.com/mnras/article/468/3/2532/3072846 by Biblioteca di Scienze tecnologiche user on 30 December 2020

Table 2. Best-fitting parameters for all the 19 dust grain models using the *Two Dust Layers with Wing* model. $x_{\rm high/low,\,1/2}$ and $N_{\rm H,\,1/2}$ are the fractional distances and $N_{\rm H,\,sca}$ of the two dust layers, as shown in Fig. 7. The COMP-AC-S dust grain model (indicated by †) was recommended for the GC direction by Fritz et al. (2011). *l*: the parameter pegs at the lower limit. χ^2/dof (ALL) is for the simultaneous fitting to all the six radial profiles in Fig. 9, while χ^2/dof (CXO) is the fitting statistics of the three *Chandra* radial profiles. Error bars are calculated for the 90 per cent confidence range. We emphasize that systematic uncertainties are more important, such as the scatter of best-fitting parameters between different dust grain models.

No.	Dust model	$x_{\rm low,\,2}$	$x_{\rm high,\,2}$	$x_{\rm low,\,1}$	$x_{\rm high,\,1}$	$N_{\rm H,\,2}$ (10^{22} cm^{-2})	$N_{\rm H,\,1}$ (10^{22} cm^{-2})	χ^2/dof (ALL)	χ^2/dof (CXO)
0	MRN77	0^l	$0.8949^{+0.0138}_{-0.0716}$	$0.9783^{+0.0010}_{-0.0021}$	$0.9976^{+0.0008}_{-0.0004}$	$13.2^{+1.1}_{-1.1}$	$6.8^{+0.9}_{-0.9}$	199/131	97/83
1	BARE-GR-S	0^l	$0.8092^{+0.0082}_{-0.0643}$	$0.9553^{+0.0022}_{-0.0062}$	$0.9975^{+0.0017}_{-0.0030}$	$9.5^{+0.5}_{-0.5}$	$2.3^{+0.3}_{-0.3}$	204/131	126/83
2	BARE-GR-FG	0^l	$0.8314^{+0.0131}_{-0.0472}$	$0.9611^{+0.0034}_{-0.0084}$	$0.9989^{+0.0011}_{-0.0006}$	$10.5^{+0.8}_{-0.8}$	$3.0^{+0.5}_{-0.5}$	198/131	107/83
3	BARE-GR-B	0^l	$0.9010^{+0.0046}_{-0.0421}$	$0.9760^{+0.0024}_{-0.0087}$	$0.9984^{+0.0011}_{-0.0003}$	$15.1^{+0.9}_{-0.9}$	$4.8^{+0.5}_{-0.5}$	169/131	94/83
4	COMP-GR-S	0^l	$0.6242^{+0.0035}_{-0.0423}$	$0.9403^{+0.0102}_{-0.0026}$	$0.9985^{+0.0014}_{-0.0001}$	$12.0^{+0.8}_{-0.8}$	$5.2^{+0.5}_{-0.5}$	230/131	100/83
5	COMP-GR-FG	0^l	$0.7465^{+0.0117}_{-0.0209}$	$0.9523^{+0.0076}_{-0.0036}$	$0.9976^{+0.0011}_{-0.0001}$	$11.6^{+0.7}_{-0.7}$	$4.9^{+0.5}_{-0.5}$	229/131	97/83
6	COMP-GR-B	0^l	$0.7913^{+0.0116}_{-0.0152}$	$0.9557^{+0.0040}_{-0.0070}$	$0.9986^{+0.0008}_{-0.0006}$	$11.3^{+0.8}_{-0.8}$	$3.2^{+0.5}_{-0.5}$	207/131	113/83
7	BARE-AC-S	0^l	$0.8491^{+0.0143}_{-0.0193}$	$0.9637^{+0.0039}_{-0.0088}$	$0.9976^{+0.0023}_{-0.0005}$	$9.6^{+0.6}_{-0.6}$	$3.2^{+0.3}_{-0.3}$	196/131	101/83
8	BARE-AC-FG	0^l	$0.8394^{+0.0218}_{-0.0172}$	$0.9625^{+0.0040}_{-0.0089}$	$0.9977^{+0.0022}_{-0.0004}$	$9.3^{+0.5}_{-0.5}$	$3.1^{+0.3}_{-0.3}$	198/131	104/83
9	BARE-AC-B	0^l	$0.8783^{+0.0283}_{-0.0561}$	$0.9665^{+0.0017}_{-0.0088}$	$0.9982^{+0.0009}_{-0.0010}$	$11.3^{+0.6}_{-0.6}$	$3.0^{+0.3}_{-0.3}$	184/131	109/83
10	COMP-AC-S†	0^l	$0.5143^{+0.0092}_{-0.5143}$	$0.9389^{+0.0060}_{-0.0208}$	$0.9978^{+0.0009}_{-0.0001}$	$13.4^{+1.3}_{-1.3}$	$5.8^{+0.8}_{-0.8}$	224/131	103/83
11	COMP-AC-FG	0^l	$0.6737^{+0.0067}_{-0.2864}$	$0.9474^{+0.0040}_{-0.0180}$	$0.9977^{+0.0009}_{-0.0001}$	$12.6^{+0.8}_{-0.8}$	$5.4^{+0.5}_{-0.5}$	239/131	105/83
12	COMP-AC-B	0^l	$0.2954^{+0.0025}_{-0.2954}$	$0.9225^{+0.0127}_{-0.0175}$	$0.9976^{+0.0018}_{-0.0009}$	$23.3^{+1.1}_{-1.1}$	$6.4^{+0.7}_{-0.7}$	213/131	137/83
13	COMP-NC-S	0^l	$0.3356^{+0.0059}_{-0.3356}$	$0.9306^{+0.0025}_{-0.0358}$	$0.9979^{+0.0012}_{-0.0002}$	$15.5^{+1.0}_{-1.0}$	$6.5^{+0.7}_{-0.7}$	234/131	121/83
14	COMP-NC-FG	0^l	$0.1093^{+0.0125}_{-0.1093}$	$0.9071^{+0.0072}_{-0.0234}$	$0.9991^{+0.0004}_{-0.0002}$	$16.2^{+1.3}_{-1.3}$	$5.4^{+0.7}_{-0.7}$	211/131	136/83
15	COMP-NC-B	0^l	$0.0100^{+0.0273}_{l}$	$0.8873^{+0.0161}_{-0.0194}$	$0.9990^{+0.0005}_{-0.0001}$	$17.9^{+1.2}_{-1.2}$	$5.9^{+0.7}_{-0.7}$	271/131	169/83
16	WD01-A	0^l	$0.8302^{+0.0086}_{-0.1314}$	$0.9628^{+0.0039}_{-0.0239}$	$0.9975^{+0.0017}_{-0.0001}$	$8.4^{+0.5}_{-0.5}$	$4.5^{+0.3}_{-0.3}$	246/131	97/83
17	WD01-B	0^l	$0.4035^{+0.0122}_{-0.4035}$	$0.9326^{+0.0027}_{-0.0243}$	$0.9977^{+0.0011}_{-0.0001}$	$3.6^{+0.2}_{-0.2}$	$1.4^{+0.1}_{-0.1}$	235/131	116/83
18	XLNW	0^l	$0.8772^{+0.0034}_{-0.0517}$	$0.9701^{+0.0088}_{-0.0065}$	$0.9974^{+0.0019}_{-0.0004}$	$11.6^{+0.6}_{-0.6}$	$4.3^{+0.4}_{-0.4}$	175/131	88/83
	min. value	0^l	0.0100^l	0.8873	0.9974	3.6	1.4	–	–
	max. value	0^l	0.9010	0.9783	0.9991	23.3	6.8	–	–
	mean value	0^l	0.6429	0.9479	0.9980	12.4	4.5	–	–
	median value	0^l	0.7913	0.9523	0.9977	11.6	4.5	–	–

~15 per cent flux uncertainty in the 5-10 keV band, which is much smaller than what we found in AX J1745.6−2901 due to the dust-scattering halo.

To quantify the spectral discrepancy, we fit the two spectra within 2–10 keV using a simple absorbed power-law model (XSPEC model: TBNEW*POWERLAW), with cross-sections of Verner et al. (1996) and WAM00 ISM abundances. For the same $N_{\rm H,\,abs}$, the best-fitting photon index differs by 0.3 (or 6σ) between the two spectra, while the flux differs by 30 per cent, 21 per cent and 9 per cent in the 2–4, 4–6 and 6–10 keV bands, respectively (see Table 4), suggesting that the spectral dependence on the source extraction region is very significant and so must be addressed properly.

5.2 Spectral correction for the dust-scattering halo

Based on the best-fitting two-layer model, we can perform corrections on the spectral effect of the dust-scattering halo. We assume the PSF correction has been performed on the spectra extracted from different annulus regions, so the spectral correction is essentially the correction for the difference between the observed source radial profile and the radial profile of the instrumental PSF, with the same flux in the source extraction region. Therefore, this correction only requires well-constrained radial profiles of the source at various energies, but does not require the knowledge about intrinsic properties of the intervening dust.

We defined the spectral correction factor as $F_{\rm int,\,E}/F_{\rm obs,\,E}$, where $F_{\rm obs,\,E}$ and $F_{\rm int,\,E}$ are the flux at energy E before and after the dust-scattering correction, and used the best-fitting model with the COMP-AC-S dust grain to calculate the correction factor. Fig. 12 shows the correction factor as a function of energy for different source extraction regions. A bigger correction factor is found at lower energies with smaller extraction regions because in this case, a bigger halo flux loss is expected. Therefore, for instruments such as *Chandra* ACIS, where a small source extraction regions is often used, it is more important to consider the spectral effect of the dust-scattering halo (Corrales et al. 2016; Smith et al. 2016).

Based on the spectral correction factor in Fig. 12, we can correct the observed spectra for the dust-scattering halo and produce a 'dust-free' spectrum. Fig. 11 shows that the two spectra from different source extraction regions become consistent with each other after the spectral correction. However, this correction to the spectral file itself is only approximate as it does not incorporate the full response profile of every energy channel in EPIC-pn, and so the most appropriate way is to correct the model rather than the spectral file. Therefore, we built an XSPEC multiplicative model (AXJDUST) for the dust-scattering halo around AX J1745.6−2901 for different annulus regions and instruments.[12] We found that adding

[12] AXJDUST model will be uploaded to the XSPEC website.

Downloaded from https://academic.oup.com/mnras/article/468/3/2532/3072846 by Biblioteca di Scienze tecnologiche user on 30 December 2020

Table 3. Parameters calculated from the best-fitting models in Table 2 with propagated statistical errors. τ is the dust-scattering optical depth calculated from each of the best-fitting models. $f_{N_{\rm H,2}} = N_{\rm H,2}/(N_{\rm H,1} + N_{\rm H,2}) \times 100$ per cent, where $N_{\rm H,1}$ and $N_{\rm H,2}$ are the $N_{\rm H,sca}$ in layer-1 and layer-2, separately. $f_{N_{\rm H,2}}$ indicates the percentage of dust contained in layer-2 along the LOS.

No.	Dust model	$x_{\rm low,1} - x_{\rm high,2}$	$N_{\rm H,2} + N_{\rm H,1}$ (10^{22} cm^{-2})	$f_{N_{\rm H,2}}$ (per cent)	τ(2 − 4 keV)	τ(4–6 keV)	τ(6–10 keV)
0	MRN77	$0.0834^{+0.0716}_{-0.0140}$	$20.0^{+1.4}_{-1.4}$	$66.0^{+3.5}_{-3.5}$	0.80	0.53	0.41
1	BARE-GR-S	$0.1461^{+0.0643}_{-0.0103}$	$11.8^{+0.6}_{-0.6}$	$80.5^{+2.2}_{-2.2}$	0.51	0.28	0.18
2	BARE-GR-FG	$0.1297^{+0.0473}_{-0.0156}$	$13.5^{+0.9}_{-0.9}$	$77.8^{+3.2}_{-3.2}$	0.65	0.42	0.32
3	BARE-GR-B	$0.0750^{+0.0421}_{-0.0098}$	$19.9^{+1.0}_{-1.0}$	$75.9^{+2.2}_{-2.2}$	0.66	0.40	0.28
4	COMP-GR-S	$0.3161^{+0.0960}_{-0.0044}$	$17.2^{+0.9}_{-0.9}$	$69.8^{+2.5}_{-2.5}$	0.93	0.65	0.53
5	COMP-GR-FG	$0.2058^{+0.0222}_{-0.0122}$	$16.5^{+0.9}_{-0.9}$	$70.3^{+2.5}_{-2.5}$	0.79	0.51	0.37
6	COMP-GR-B	$0.1644^{+0.0157}_{-0.0135}$	$14.5^{+0.9}_{-0.9}$	$77.9^{+3.0}_{-3.0}$	0.61	0.38	0.28
7	BARE-AC-S	$0.1146^{+0.0197}_{-0.0168}$	$12.8^{+0.7}_{-0.7}$	$75.0^{+2.1}_{-2.1}$	0.63	0.37	0.26
8	BARE-AC-FG	$0.1231^{+0.0177}_{-0.0235}$	$12.4^{+0.6}_{-0.6}$	$75.0^{+2.1}_{-2.1}$	0.62	0.37	0.25
9	BARE-AC-B	$0.0882^{+0.0561}_{-0.0296}$	$14.3^{+0.7}_{-0.7}$	$79.0^{+1.9}_{-1.9}$	0.57	0.33	0.23
10	COMP-AC-S†	$0.4246^{+0.5143}_{-0.0227}$	$19.2^{+1.5}_{-1.5}$	$69.8^{+3.6}_{-3.6}$	0.82	0.55	0.43
11	COMP-AC-FG	$0.2737^{+0.2864}_{-0.0192}$	$18.0^{+0.9}_{-0.9}$	$70.0^{+2.4}_{-2.4}$	0.77	0.50	0.37
12	COMP-AC-B	$0.6271^{+0.2957}_{-0.0177}$	$29.7^{+1.3}_{-1.3}$	$78.5^{+2.0}_{-2.0}$	0.55	0.33	0.22
13	COMP-NC-S	$0.5950^{+0.3356}_{-0.0363}$	$22.0^{+1.2}_{-1.2}$	$70.5^{+2.6}_{-2.6}$	0.78	0.53	0.41
14	COMP-NC-FG	$0.7978^{+0.1095}_{-0.0265}$	$21.6^{+1.5}_{-1.5}$	$75.0^{+2.9}_{-2.9}$	0.85	0.63	0.52
15	COMP-NC-B	$0.8773^{+0.0189}_{-0.0335}$	$23.8^{+1.4}_{-1.4}$	$75.2^{+2.5}_{-2.5}$	0.71	0.48	0.38
16	WD01-A	$0.1326^{+0.1315}_{-0.0254}$	$12.9^{+0.6}_{-0.6}$	$65.1^{+2.0}_{-2.0}$	1.07	0.76	0.61
17	WD01-B	$0.5291^{+0.4035}_{-0.0272}$	$5.0^{+0.2}_{-0.2}$	$72.0^{+1.8}_{-1.8}$	0.75	0.51	0.40
18	XLNW	$0.0929^{+0.0524}_{-0.0073}$	$15.9^{+0.7}_{-0.7}$	$73.0^{+2.1}_{-2.1}$	0.71	0.43	0.30
	min. value	0.0882	5.0	66.0	0.51	0.28	0.18
	max. value	0.8773	29.7	80.5	1.07	0.76	0.61
	mean value	0.3051	16.9	74.4	0.73	0.47	0.36
	median value	0.1644	16.5	75.0	0.71	0.48	0.37

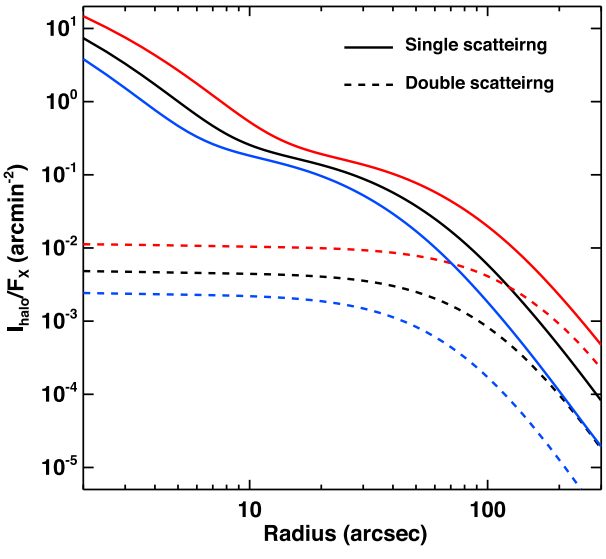


Figure 10. Comparison of the radial profiles from the single scattering (solid lines) and double scattering (dashed lines) for 3.3 (red, $\tau = 0.82$), 5.0 (black, $\tau = 0.55$) and 7.0 keV (blue, $\tau = 0.42$), based on the two-layer model with COMP-AC-S dust grains (Table 3).

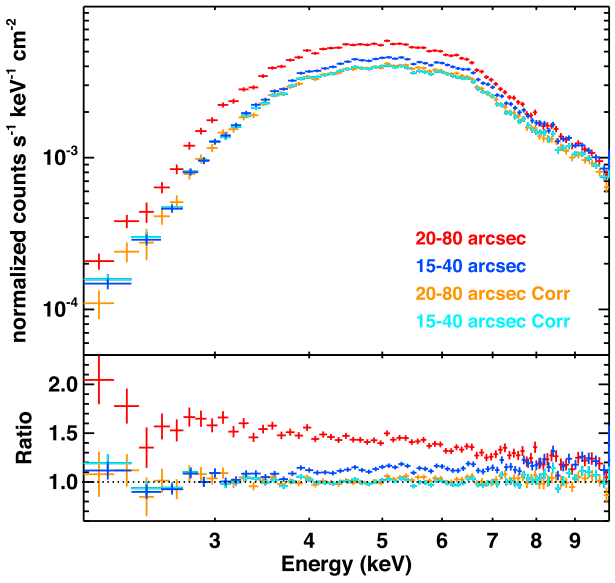


Figure 11. *XMM–Newton* EPIC-pn spectra of AX J1745.6−2901 from different extraction regions (ObsID: 0724210201). The red spectrum is from a 20–80 arcsec annulus region, which is both significantly brighter and softer than the blue spectrum from a 15–40 arcsec annulus region. Both spectra have been corrected for the same EPIC-pn PSF. The spectral difference is essentially caused by the dust-scattering halo, which can be corrected for using our dust-scattering model (i.e. the consistent orange and cyan spectra, see Section 5.2). Lower panel shows the ratio of the four spectra to the best-fitting absorbed power-law model to the orange spectrum.

this model component can fully account for the spectral discrepancy in Fig. 11 and produce consistent best-fitting parameters from the two apparently different spectra. The best-fitting parameters also change significantly after the inclusion of AXJDUST model (see

Downloaded from https://academic.oup.com/mnras/article/468/3/2532/3072846 by Biblioteca di Scienze tecnologiche user on 30 December 2020

Table 4. Comparison of the best-fitting parameters for the two spectra in Fig. 11, fitted using the TBNEW*POWERLAW model in XSPEC within 2–10 keV. 'Corr' indicates whether the AXJDUST model for the dust-scattering opacity correction is incorporated or not. Including the AXJDUST model enables us to obtain consistent spectral parameters from the two very different spectra.

Spectrum (arcsec)	Corr.	[a]$N_{\rm H,\,abs}$ (10^{22} cm^{-2})	Γ	Norm	$F_{2-4\,\rm keV}$	$F_{4-6\,\rm keV}$ (10^{-12} erg cm^{-2} s^{-1})	$F_{6-10\,\rm keV}$	χ^2/dof
Spec (15–40)	no	40.9 ±0.6	3.06 ±0.04	1.65 ±0.1	15.2 ±0.1	68.4 ±0.4	97.8 ±0.5	1866/1359
Spec (20–80)	no	40.5 ±0.4	3.38 ±0.04	3.46 ±0.3	21.8 ±0.1	86.3 ±0.5	107.3 ±0.6	1916/1409
Spec (15–40)	yes	38.8 ±0.6	3.01 ±0.04	1.30 ±0.12	14.1 ±0.1	60.7 ±0.3	88.6 ±0.5	1827/1359
Spec (20–80)	yes	39.1 ±0.6	3.06 ±0.04	1.46 ±0.13	14.5 ±0.1	62.3 ±0.3	89.5 ±0.5	1942/1409

[a] This $N_{\rm H,\,abs}$ does not necessarily reflect the true $N_{\rm H,\,abs}$ of AX J1745.6−2901, because the absorbed power-law model is not a good model for the entire 2–10 keV band (see Section 5.2).

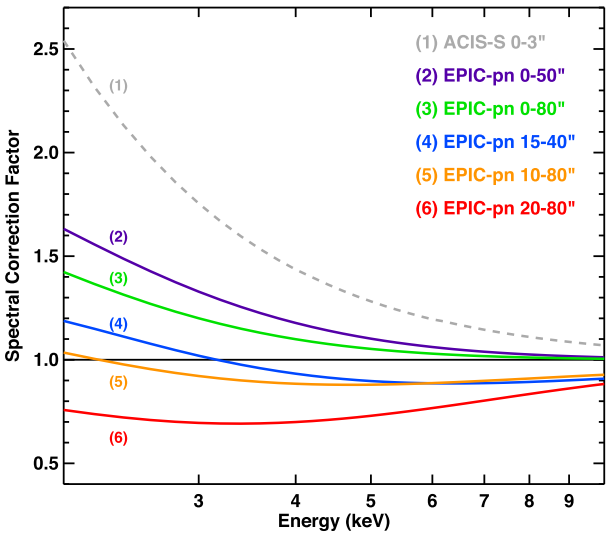


Figure 12. Energy-dependent spectral correction factor for the dust-scattering opacity (Section 5.2) for various instruments and spectral extraction regions. Note that these curves are only for the dust on the LOS of AX J1745.6−2901.

Table 4). Since the absorbed power-law model is clearly not good enough for the entire 2–10 keV band, we restrict the fitting to 3–6 keV band and we find a much better fit with $\chi^2/ = 595/596$, $N_{\rm H,\,abs} = (3.02 \pm 0.17) \times 10^{23}$ cm^{-2} and $\Gamma = 2.02 \pm 0.17$. These parameters are also roughly consistent with those reported by Paizis et al. (2015) using the lower S/N *Chandra* HETG spectrum and applying the same absorbed power-law model with the same cross-sections and abundances.

Furthermore, to assess the contribution from different dust layers, we calculated the spectral correction factor assuming there is only dust layer-1 or layer-2, separately. It is found that the bias is mainly caused by dust layer-2, which is far from AX J1745.6−2901 (Fig. 13). This is because dust layer-1 is so close to AX J1745.6−2901 that its halo is very compact and its shape is very similar to the instrumental PSF (see Fig. 9), and so the PSF correction also corrects for the halo flux loss with small biases. Dust layer-2 is far from AX J1745.6−2901, and so it produces an extended dust-scattering halo, which is more extended than the instrumental PSF and is also more difficult to be covered by a small spectral extraction region, thereby requiring a more significant correction factor.

6 DISCUSSION

6.1 Dust distribution in the GC direction

Interstellar dust is typically contained in molecular clouds, whose spatial distribution can be traced by molecular lines (e.g. CO emission; Dame, Hartmann & Thaddeus 2001). Previous Galactic CO maps showed a prominent feature due to a massive molecular ring at 4–5 kpc from the GC (the so-called 5 kpc molecular ring; Jackson et al. 2006; Simon et al. 2006), or 3–4 kpc from Earth in the GC direction (Valleé 2014). Later studies showed an enhancement of mass density of the molecular clouds between 3 and 6 kpc from the GC overlapping with the 5-kpc molecular ring, which also seems to be distributed along the Scutum Arm (Roman-Duval et al. 2010; Dobbs & Burkert 2012; Sato et al. 2014; Heyer & Dame 2015). Previous surveys about the IR dark clouds (Egan et al. 1998; Carey et al. 1998) found that these clouds mainly lie along the Scutum arm between 3 and 6 kpc from the GC (Simon et al. 2006; Marshall, Joncas & Jones 2009) with typical $N_{\rm H} \gtrsim 10^{22}$ cm^{-2} in a single cloud (Simon et al. 2006; Peretto & Fuller 2010). Therefore, it is indeed possible for the GC LOS to contain a large amount of intervening dust about half way between the Earth and the GC.

Another method to infer the dust distribution is to use the dust extinction map. Using the IR extinction curve towards the GC, Fritz et al. (2011) reported that most of the extinction is caused by the dust in the Galactic disc rather than in the nuclear bulge (Mezger, Duschl & Zylka 1996). Voshchinnikov, Henning & Il'in (2017) also showed that the IR extinction curve can be explained by a GC dust component and a foreground dust component. Schultheis et al. (2014) built a 3D dust extinction map for the Galactic bulge and found a peak of extinction at 3 kpc from the GC, implying a dust lane in front of the Galactic bar, but they cannot rule out the possibility that this peak is associated with the 5-kpc molecular ring.

All the above studies consistently show that most of the dust is distributed several kpc from the GC in the Galactic disc. This invalidates the assumption made in Tan & Draine (2004), where the dust-scattering halo from Sgr A* was assumed to rise from the intervening dust and gas close to Sgr A*. Interestingly, recent studies of PSR J1745−2900, the magnetar located at only 2.4 arcsec from Sgr A* (Kennea et al. 2013; Mori et al. 2013; Rea et al. 2013), also show that most of the scattering medium responsible for the broadening of the radio emission from this magnetar is likely associated with the interstellar gas in the Galactic disc, possibly in a nearby spiral arm, rather than close to the GC (Eatough et al. 2013; Shannon & Johnston 2013; Bower et al. 2014; Wucknitz 2015; Sicheneder & Dexter 2017; but see Spitler et al. 2014).

Downloaded from https://academic.oup.com/mnras/article/468/3/2532/3072846 by Biblioteca di Scienze tecnologiche user on 30 December 2020

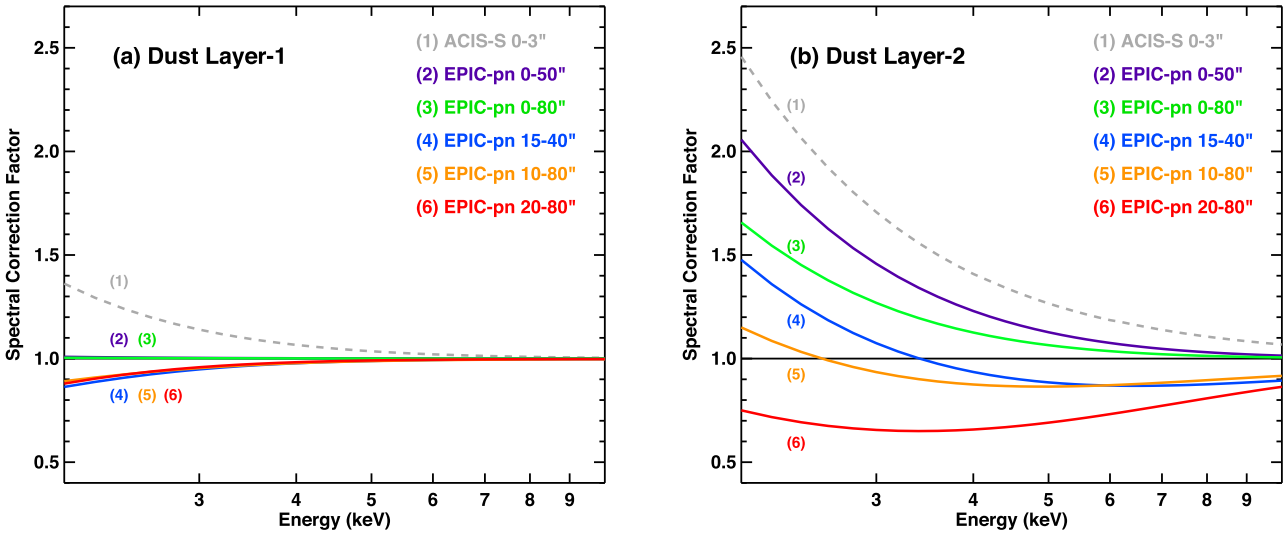


Figure 13. Energy-dependent spectral correction factor for the two dust layers for various instruments and spectral extraction regions, based on the best-fitting parameters with the COMP-AC-S dust grains (Table 2). Panel (a) is for layer-1, which is local to AX J1745.6−2901; Panel (b) is for layer-2, which is far from AX J1745.6−2901. It is clear that layer-2 introduces much bigger spectral biases than layer-1.

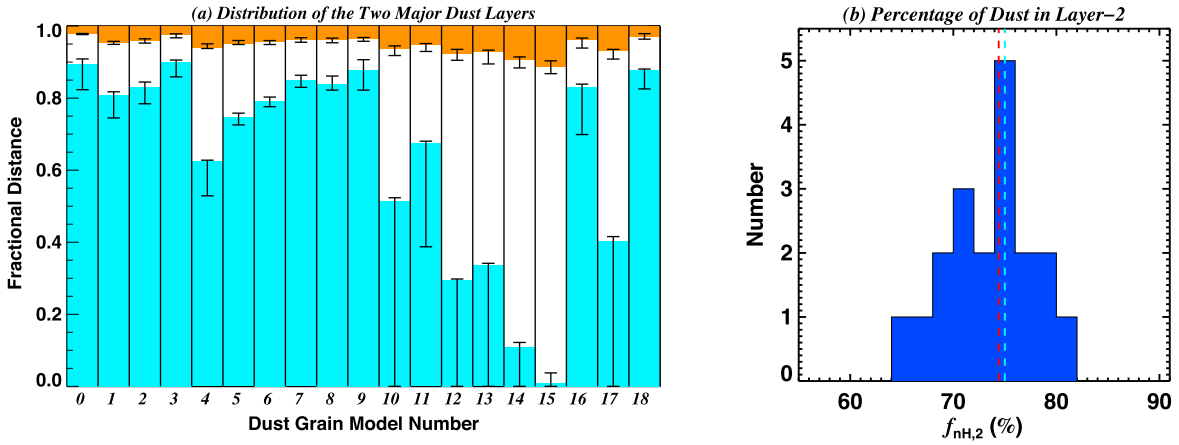


Figure 14. Panel (a): the distribution of the two major dust layers along the LOS, with the orange region being layer-1 and cyan region being layer-2. Distance 0 corresponds to the Earth, while distance 1 corresponds to AX J1745.6−2901. Error bars indicate the statistical uncertainty of each layer's boundary. Significant separation between the two layers can be found in very dust grain model. Panel (b): the distribution of the percentage of LOS dust in dust layer-2. The red and cyan dashed lines indicate the mean value of 74.4 per cent and median value of 75.0 per cent, separately. Dust grain model number and all the data can be found in Tables 2 and 3.

Our study on AX J1745.6−2901 is the first detailed observation and modelling of a dust-scattering halo around a source in the GC. The dust properties and distribution of the two major layers show a large dispersion, which is mainly due to the lack of knowledge about the properties of dust grains in the ISM especially along the GC LOS. But there are some robust results that can be derived from all the dust grain models. First, although the separation between the two major layers changes from 0.09 to 0.88 (with mean value: 0.31) for different dust grain models, all the models consistently find a highly significant separation between the two layers (see Fig. 14a), i.e. layer-1 is always found to be local to AX J1745.6−2901, while layer-2 is significantly far away and always has its lower boundary reaching 0. Secondly, we find that the percentage of dust that is contained in each layer is tightly constrained and it is observed to be (66–81) per cent (with mean value: 74.4 per cent) in layer-2, with a much weaker dependence on the dust grain models than the other parameters (see Fig. 14b). We emphasize that an extra uncertainty of this dust distribution lies in the assumption of the same type of dust grains in different dust layers. It has been reported that the abundances in the GC may be higher than in the Galactic disc (see Section 6.2 for a more detailed discussion), and the GC dust grains might have a smaller characteristic size (Hankins et al. 2017). However, there are no strong constraints on these GC parameters, and we are not sure if AX J1745.6−2901 is located inside the GC region or not (see discussions below), thus, in this work, we do not consider different dust grain models for different dust layers.

The absolute location of these two layers also depends on the absolute distance of AX J1745.6−2901 itself, which is still highly uncertain. From the fact that the $N_{\rm H,\,abs}$ of AX J1745.6−2901 is significantly larger than that of Sgr A* (fusing the same absorption model and abundances, see Section 1.3), it can be reasonably inferred that AX J1745.6−2901 is NOT closer to the Earth

Downloaded from https://academic.oup.com/mnras/article/468/3/2532/3072846 by Biblioteca di Scienze tecnologiche user on 30 December 2020

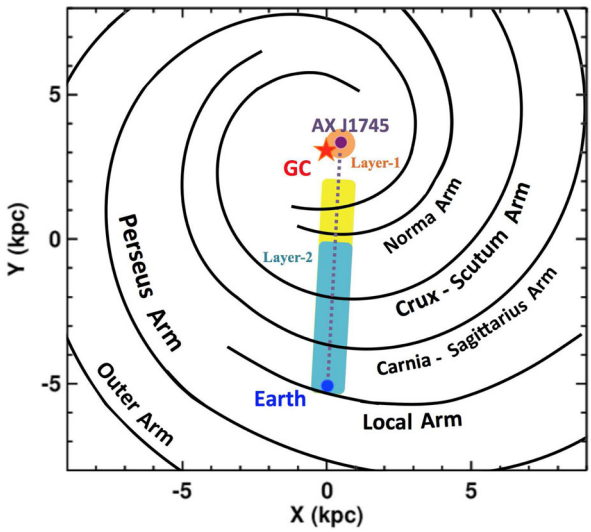


Figure 15. Schematic of the Milky Way spiral arms viewed from the north Galactic pole based on the Milky Way structure reported by Nakanishi & Sofue (2016), Reid et al. (2009) and Caswell & Haynes (1987). The orange and dark green regions indicate the location of dust layer-1 and dust layer-2 based on the average best-fitting parameters in Table 2, assuming AX J1745.6−2901 is in the GC. The yellow region shows the highest upper boundary (0.9) of dust layer-2 from the fitting using the BARE-GR-B dust grain model.

than Sgr A*. Although $N_{\rm H,\,sca}$ is not directly comparable to the $N_{\rm H,\,abs}$ as they have different normalizations (see Section 6.2), by assuming the same dust properties in all the layers, we can use the fraction of dust to infer the fraction of $N_{\rm H,\,abs}$ in each layer. Therefore, adopting $N_{\rm H,\,abs} = 3 \times 10^{23}\,{\rm cm}^{-2}$ for AX J1745.6−2901 (see Section 5.2) and $1.6 \times 10^{23}\,{\rm cm}^{-2}$ for Sgr A* from the TBNEW model and WAM00 abundances (Ponti et al. 2017b), we can estimate $N_{\rm H,\,abs} = (2.0\text{–}2.4) \times 10^{23}\,{\rm cm}^{-2}$ in layer-2, which is similar to Sgr A*. This is also consistent with the fact that layer-1 is local to AX J1745.6−2901 and layer-2 is much farther away, thus it is likely that only layer-2 is in front of Sgr A*.

If a distance of 8 kpc is adopted for AX J1745.6−2901, the mean fractional distance of layer-2 would indicate that it is 0–5 kpc from the Earth in the Galactic disc, thus it overlaps with the Crux-Scutum Arm, Carnia-Sagittarius Arm and the local Arm (see Fig. 15; Caswell & Haynes 1987; Reid et al. 2009; Nakanishi & Sofue 2016). This result immediately implies the possibility that the same dust in layer-2 may also intervene along the LOS of many GC sources. There are two X-ray transients whose LOSs are very close to Sgr A*. Swift J174540.7−290015 was discovered in 2016 at 16 arcsec from Sgr A* (Reynolds et al. 2016), with $N_{\rm H,\,abs} = 1.7 \times 10^{23}\,{\rm cm}^{-2}$ (TBNEW model and WAM00 abundances; Ponti et al. 2016). SGR J1745−2900 is located at 2.4 arcsec from Sgr A* (Rea et al. 2013), with $N_{\rm H,\,abs} = 1.9 \times 10^{23}\,{\rm cm}^{-2}$ (TBABS model and WAM00 abundances; Coti-Zelati et al. 2015). Although a further correction for the dust-scattering opacity is probably also necessary for these GC sources, their $N_{\rm H,\,abs}$ are indeed similar to that of layer-2 (also see Ponti et al. 2017b), which support layer-2 being a common GC-foreground dust layer in the Galactic disc. A more conclusive study would be to compare the dust-scattering haloes around many GC sources and see if a similar dust component as layer-2 exists in their halo profiles.

6.2 Testing dust-to-gas relations in the GC direction

Since $\tau_{\rm sca}$, $N_{\rm H,\,sca}$ and $N_{\rm H,\,abs}$ have all been measured independently in AX J1745.6−2901, it becomes the first source that allows the test of dust-to-gas relations in the GC LOS. However, we would like to emphasize that there are some underlying systematic uncertainties associated with the $N_{\rm H}$ measurement. First, $N_{\rm H,\,sca}$ depends heavily on the assumptions made in the dust grain models such as the abundances and the grain size distribution, which affect the halo intensity and profile, which then affect $N_{\rm H,\,sca}$ during the halo profile fitting. This is why a large dispersion of $N_{\rm H,\,sca}$ is found among all the dust grain models. Secondly, $N_{\rm H,\,abs}$ also depends heavily on the assumed abundances during the X-ray spectral fitting. In the case of AX J1745.6−2901, we found ∼50 per cent change in $N_{\rm H,\,abs}$ by simply changing the abundances from the AG89 solar abundances to WAM00 ISM abundances. Moreover, $N_{\rm H,\,abs}$ depends on the absorption model and intrinsic spectral model used for the spectral fitting. A high S/N and resolution spectra with a good intrinsic model would allow the absorption model to determine $N_{\rm H,\,abs}$ from various metal absorption edges; while a low S/N spectra or a bad intrinsic model would force the absorption model to trace the spectral curvature (as likely in AX J1745.6−2901 and many other GC sources where the strong extinction leads to a fast decrease of S/N in the soft X-ray band), which would bias $N_{\rm H,\,abs}$. Therefore, it is not meaningful to do a precise comparison between $N_{\rm H,\,sca}$ and $N_{\rm H,\,abs}$. Actually, some of the dust and gas in layer-1 can be so close to AX J1745.6−2901 that they would absorb X-rays but not *observably* scatter them, and so the *observed* $N_{\rm H,\,sca}$ should be smaller than the intrinsic $N_{\rm H}$. It must also be stressed that it is necessary to provide key information when an $N_{\rm H,\,abs}$ is reported, such as the quality of spectra being fitted, models used for the intrinsic spectra and X-ray absorption, and assumptions made for the cross-sections and abundances.

On the other hand, several versions of the dust-to-gas relations between $N_{\rm H,\,abs}$, A_V and $\tau_{\rm sca}$ have been reported so far. For example, Predehl & Schmitt (1995) (hereafter PS95) performed X-ray spectral and halo fittings for 25 point sources observed by *ROSAT* and reported $N_{\rm H,\,abs}/A_V = 1.79 \times 10^{21}\,{\rm cm}^{-2}\,{\rm mag}^{-1}$ and $\tau_{\rm sca} = 0.087 \times A_V({\rm mag})\,E({\rm keV})^{-2}$. Their absorption model used the Morrison & McCammon (1983) cross-sections, which is equivalent to the XSPEC WABS model. However, Draine & Bond (2004) (hereafter DB04) argued that Predehl & Schmitt (1995) may have underestimated the scattering power and so a better relation would be $\tau_{\rm sca} = 0.15 \times A_V({\rm mag})\,E({\rm keV})^{-1.8}$. Later, Güver & Özel (2009) (hereafter LO09) collected 22 supernova remnants that have their $N_{\rm H,\,abs}$ measured from the high-quality X-ray spectra from *Chandra*, *XMM–Newton* and *Suzaku*, and have independent A_V measurements. They reported $N_{\rm H,\,abs}/A_V = (2.21 \pm 0.09) \times 10^{21}\,{\rm cm}^{-2}\,{\rm mag}^{-1}$. Their difference from Predehl & Schmitt (1995) was attributed to the narrow bandpass of *ROSAT* and the simple power-law model assumed for the intrinsic spectra. However, it is difficult to track down all the absorption models, cross-sections and abundances used to derive the $N_{\rm H,\,abs}$ of their sample because they were reported by many different papers and authors. Recently, Valencic & Smith (2015) (hereafter VS15) analysed the X-ray dust-scattering halo around 35 sources and found $N_{\rm H,\,abs}/A_V = (2.08 \pm 0.26) \times 10^{21}\,{\rm cm}^{-2}{\rm mag}^{-1}$, with $\tau_{\rm sca}(1.0keV)/A_V$ having a typical $\pm 1\sigma$ range of 0.02–0.08 depending on the dust grain model. Their $N_{\rm H,\,abs}$ was based on the AG89 solar abundances and PHABS model.

In order to use these relations, we adopt $N_{\rm H,\,abs} \simeq 2 \times 10^{23}\,{\rm cm}^{-2}$ for AX J1745.6−2901, also based on the PHABS model and the AG89 solar abundances. It is known that the metallicity near/in the

Downloaded from https://academic.oup.com/mnras/article/468/3/2532/3072846 by Biblioteca di Scienze tecnologiche user on 30 December 2020

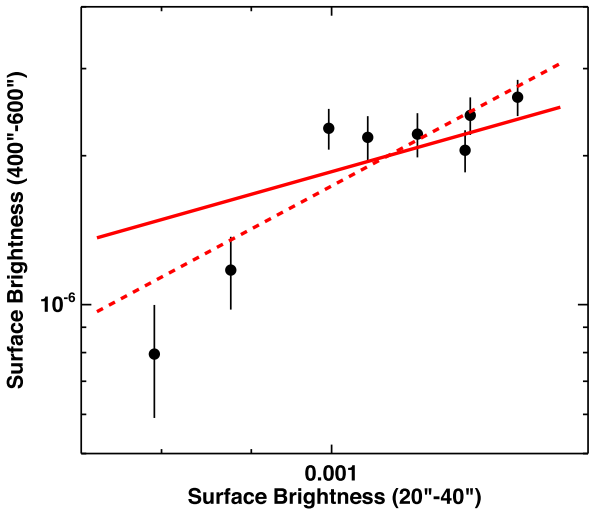


Figure 16. The correlation between the halo wing and halo core intensity in the 4–6 keV band. The unit for the surface brightness is counts $cm^{-2}\,s^{-1}\,arcmin^{-2}$. The data points are measured from the eight *XMM–Newton* observations in Table 1. The red solid line is the best-fitting line assuming a slope of 1, the red dashed line is the best-fitting line with the best-fitting slope of 1.9 ± 0.5.

GC is higher than the solar abundances (e.g. Kubryk, Prantzos & Athanassoula 2015, and references therein). If some of the dust and gas in, for example, layer-1 is indeed close to the GC, the $N_{\rm H,\,abs}$ from the AG89 abundances would have been overpredicted. However, it is also reported that the AG89 metallicity overestimated the solar metallicity (e.g. Asplund et al. 2009; Nieva & Przybilla 2012), thus the adoption of AG89 abundances may actually alleviate the potential higher metallicity problem towards AX J1745.6−2901. We find $A_V = 117, 90, 96$ mag from the $N_{\rm H,\,abs}/A_V$ relations in PS95, LO09 and VS15, respectively. Adopting $A_V \simeq 100$ mag, we derive $\tau_{\rm sca} = 0.80, 0.35$ and 0.18 at 3.3, 5.0 and 7.0 keV from the $\tau_{\rm sca}/A_V$ relation in PS95, or $\tau_{\rm sca} = 1.75, 0.83$ and 0.45 from DB04, or $\tau_{\rm sca} = 0.73, 0.32$ and 0.16 from VS15. Therefore, it appears that the dust-to-gas relations in PS95 and VS15 give more consistent $\tau_{\rm sca}$ with those measured directly from the eclipsing light curves.

6.3 Excess flux in the halo wing

In this work, we reported, for the first time, the detection of a significant wing of the dust-scattering halo at $E \geq 5$ keV. On the other hand, previous studies about the dust-scattering halo mainly focused on energies below 3 keV (e.g. Predehl & Schmitt 1995; Xiang et al. 2005; VS15), and used a free constant to fit the underlying background, hampering the distinguishing of an extended halo wing even if it existed. This is possible in our work because the background is well constrained from observations where AX J1745.6−2901 was in quiescence, which then enabled us to detect this excess flux in the halo wing.

In order to verify that this halo wing is related to the scattering light from AX J1745.6−2901, we tested the correlation between the flux of the halo wing and the flux of the halo core using all the *XMM–Newton* observations in Table 1. Fig. 16 shows that a clear correlation is found. The Spearman's rank correlation coefficient is 0.79 and the p-value is 0.02, and Pearson's linear correlation coefficient is 0.89. A linear fitting with slope fixed at 1 would produce a χ^2 of 7.1 for 7 dof (red solid line in Fig. 16). Freeing the slope in the fitting only improves the χ^2 by 1.0 for one extra free parameter, and the best-fitting slope is 1.9 ± 0.5 (red dashed line in Fig. 16). These results indicate that the correlation between the halo wing flux and halo core flux is consistent with a linear correlation, confirming that the wing structure in the radial profile is indeed part of the dust-scattering halo around AX J1745.6−2901.

Since smaller dust grains can scatter photons at larger angles more efficiently, this halo wing implies an excess fraction of dust grains of relatively small sizes in the ISM. According to equation (5), for a viewing angle of 300–600 arcsec at 5 keV, the typical dust grain size would be 300–590 Å, which is still two orders of magnitude bigger than the wavelength of X-ray photons (2.5 Å for 5 keV), and so the Rayleigh–Gans approximation is still valid. However, the outer boundary of the halo wing is still unknown as at larger radii, the wing starts to blend with the diffuse and background emission. If the wing is more extended than currently detected, the inferred dust grains can have smaller sizes. Therefore, the halo wing suggests a higher fraction of dust grains with typical sizes of $\lesssim$590 Å than considered in current dust grain models. This size range covers the typical sizes of PAH (3.5–55 Å; ZDA04), and is within the typical sizes of Graphite, ACH2, Olivine, Enstatite, Fe metal and the composite dust grains in ZDA04 (but is one order of magnitude smaller than the largest dust grains). Since we do not know the size distribution and composition of this dust, it is not possible to predict the influence in other aspects such as the IR emission or excitation. Future studies of the dust grain model along the GC LOS should take these halo wing phenomena into account.

6.4 Halo uniformity

The non-uniformity of dust-scattering haloes has been noticed before (McCollough, Smith & Valencic 2013; Seward & Smith 2013; VS15), which may rise from partially aligned non-spherical grains (Draine & Allaf-Akbari 2006) or azimuthal variation of the foreground dust column density. Following our previous discussion, if AX J1745.6−2901 is located inside or beyond the GC, then layer-1 is probably associated with the molecular clouds in the central molecular zone, whose column density is known to vary severely along different LOS (e.g. Serabyn & Guesten 1987; Morris & Serabyn 1996; Molinari et al. 2011; Ponti et al. 2013; Langer et al. 2015; Henshaw et al. 2016). If so, the halo produced by layer-1 might show azimuthal variation. To test this, we generated a contour map on the ACIS-S image of AX J1745.6−2901 in the 4–6 keV band (Fig. 17, based on ObsID: 17857). No obvious azimuthal variation is seen in the image except for the artificial asymmetry due to the subtraction of the readout streaks, suggesting that layer-1 should not have strong column density variation. The halo outside 20 arcsec is dominated by layer-2, and we found no clear asymmetry out to the LOS of Sgr A*either. This is supporting evidence that the same layer-2 may also intervene along the LOS to Sgr A*. Further study of the non-uniformity would require more photon counts and more careful azimuthal structure analysis (e.g. Seward & Smith 2013), which is beyond the scope of this work.

7 CONCLUSIONS

In this paper, we used a large data set from *Chandra* and *XMM–Newton* to conduct a detailed analysis of the radial profile of AX J1745.6−2901, whose LOS is ∼1.45 arcmin away from Sgr A*. Being a bright X-ray source with a high column density, this source is surrounded by a strong dust-scattering halo across the entire 2–10 keV band.

Downloaded from https://academic.oup.com/mnras/article/468/3/2532/3072846 by Biblioteca di Scienze tecnologiche user on 30 December 2020

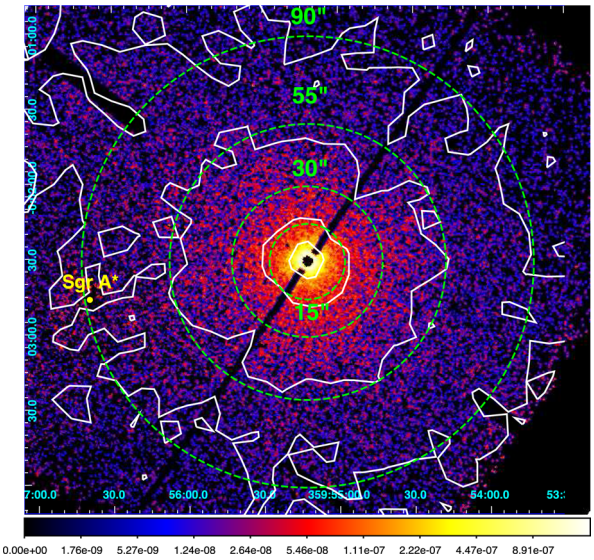


Figure 17. Background-subtracted image of AX J1745.6−2901 in the 4–6 keV band using ACIS-S observations. The vertical axis is the Galactic latitude, the horizontal axis is the Galactic longitude. The readout streaks and central 2.5 arcsec are subtracted. The white surface brightness contours are based on the same image smoothed by 15 arcsec, which shows no strong azimuthal variation except for the artificial non-uniformity due to the readout streaks.

(1) Based on the halo profile modelling, we identified two major scattering components, namely dust layer-1 and layer-2. For all the 19 dust grain models used in this work, and assuming the same dust grain model along the LOS, we found that layer-1 is produced by the dust close to AX J1745.6−2901 within a fractional distance of $\lesssim$0.11 and contains (19–34) per cent (mean value: 26 per cent) of the total LOS dust. The remaining (66–81) per cent (mean value: 74 per cent) LOS dust is contained in layer-2, distributing from the Earth up to a fractional distance of 0.01–0.90, with a mean value of 0.64 from all dust grain models. These two layers separate from each other significantly by a fractional distance of 0.08–0.88, with a mean value of 0.31. Assuming that AX J1745.6−2901 is located at 8 kpc in the GC, Layer-2 must be distributed in the Galactic disc and probably associated with the molecular clouds distributed along the spiral arms on the LOS, such as the Crux-Scutum Arm, Carnia-Sagittarius Arm and the Local Arm.

(2) In addition to the two dust-scattering components, we identified an extended component in the halo wing, which cannot be explained by any dust grain model used in this work. This halo wing suggests a higher fraction of dust grains with typical sizes of $\lesssim$590 Å than considered in current dust grain models.

(3) We also investigated the influence of the dust-scattering halo on the observed spectra. We found that the observed spectra of AX J1745.6−2901 can strongly depend on the source extraction region, which is due to the partial inclusion of the dust-scattering halo. The more extended halo from layer-2 has a stronger spectral effect. After applying the spectral correction for the dust scattering towards AX J1745.6−2901, we found $N_{\rm H,\,abs} = (3.02 \pm 0.17) \times 10^{23}$ cm^{-2} and $\Gamma = 2.02 \pm 0.17$ by fitting the TBNEW*POWERLAW model to the 3–6 keV spectrum from *XMM–Newton* EPIC-pn, with cross-sections of Verner et al. (1996) and WAM00 ISM abundances.

(4) Since layer-2 is likely associated with the dust in the Galactic disc several kpc away from AX J1745.6−2901, it may also intervene the LOS of other nearby GC sources such as Sgr A*. We found a rough consistency between the $N_{\rm H,\,abs}$ of layer-2, Sgr A* and a couple of nearby transients, so it is possible that layer-2 also produces dust scattering in these sources. A more conclusive study would be to compare the halo shapes from all these sources. If it is confirmed that the same dust population in layer-2 also intervenes other nearby LOSs towards the GC, a significant spectral correction for the dust-scattering halo would be necessary for many GC sources.

(5) We built XSPEC models to account for the spectral discrepancy caused by the entire dust-scattering halo around AX J1745.6−2901 (AXJDUST model), as well as the dust scattering in layer-2 alone (FGCDUST model). so that it can be applicable to the other sources in the GC.. These models can properly correct for different spectral discrepancies arising from different source extraction regions.[13]

ACKNOWLEDGEMENTS

We thank Elisa Costantini for helpful discussions and comments. CJ acknowledges valuable discussions with Lynne Valencic about the cosmic abundances. The anonymous referee is appreciated for providing insightful comments and suggestions, which allowed us to improve this paper significantly. We would also like to thank the *XMM–Newton* team for providing important instructions on technical and calibration issues. This project is supported by the Bundesministerium für Wirtschaft und Technologie/Deutsches Zentrum für Luft- und Raumfahrt (BMWI/DLR, FKZ 50 OR 1408 and FKZ 50 OR 1604) and the Max Planck Society. This work is based on observations obtained with *XMM–Newton*, an ESA science mission with instruments and contributions directly funded by ESA Member States and NASA. The scientific results reported in this paper are also based on observations made by the *Chandra* X-ray Observatory, as well as data obtained from the *Chandra* Data Archive. This research has made use of software provided by the *Chandra* X-ray Center (CXC) in the application packages CIAO, CHIPS and SHERPA.

REFERENCES

Anders E., Ebihara M., 1982, Geochim. Cosmochim. Acta, 46, 2363
Anders E., Grevesse N., 1989, Geochim. Cosmochim. Acta, 53, 197
Asplund M., Grevesse N., Sauval A. J., Scott P., 2009, ARA&A, 47, 481
Becklin E. E., Neugebauer G., 1968, ApJ, 151, 145
Boehle A. et al., 2016, ApJ, 830, 17
Bohren C. F., Huffman D. R., 1983, Absorption and Scattering of Light by Small Particles. Wiley, New York
Bower G. C. et al., 2014, ApJ, 780, L2
Carey S. J., Clark F. O., Egan M. P., Price S. D., Shipman R. F., Kuchar T. A., 1998, ApJ, 508, 721
Caswell J. L., Haynes R. F., 1987, A&A, 171, 261
Clavel M., Terrier R., Goldwurm A., Morris M. R., Ponti G., Soldi S., Trap G., 2013, A&A, 558, 32
Corrales L. R., Paerels F., 2015, MNRAS, 453, 1121
Corrales L. R., García J., Wilms J., Baganoff F., 2016, MNRAS, 458, 1345
Costantini E., Freyberg M. J., Predehl P., 2005, A&A, 444, 187
Coti-Zelati F. et al., 2015, MNRAS, 449, 2685
Dame T. M., Hartmann D., Thaddeus P., 2001, ApJ, 547, 792
Degenaar N., Wijnands R., 2009, A&A, 495, 547
Degenaar N., Wijnands R., Cackett E. M., Homan J., in't Zand J. J. M., Kuulkers E., Maccarone T. J., van der Klis M., 2012, A&A, 545, A49
Degenaar N., Wijnands R., Miller J. M., Reynolds M. T., Kennea J., Gehrels N., 2015, J. High Energy Astrophys., 7, 137

[13] We have created different versions of these dust-scattering models for the CCD quality spectra from *XMM–Newton* EPIC, *Chandra* ACIS, *Swift* XRT and *NuSTAR*. These models will be uploaded to the XSPEC website. Interested readers can also contact C. Jin directly for these models.

Downloaded from https://academic.oup.com/mnras/article/468/3/2532/3072846 by Biblioteca di Scienze tecnologiche user on 30 December 2020

Dobbs C. L., Burkert A., 2012, MNRAS, 421, 2940
Draine B. T., 2003, ARA&A, 41, 241
Draine B. T., Allaf-Akbari K., 2006, ApJ, 652, 1318
Draine B. T., Bond N. A., 2004, ApJ, 617, 987 (DB04)
Eatough R. P., Kramer M., Lyne A. G., Keith M. J., 2013, MNRAS, 431, 292
Egan M. P., Shipman R. F., Price S. D., Carey S. J., Clark F. O., Cohen M., 1998, ApJ, 494, L199
Fritz T. K. et al., 2011, ApJ, 737, 73
Gaetz T. J., 2010, Analysis of the Chandra On-Orbit PSF Wings, available at http://cxc.harvard.edu/cal/Hrma/PSFWings.html
Genzel R., Eisenhauer F., Gillessen S., 2010, Rev. Mod. Phys., 82, 3121
Ghizzardi S., 2002, XMM-Newton Calibration Documentation (XMM-SOC-CAL-TN-0029)
Gladstone J., Done C., Gierliński M., 2007, MNRAS, 378, 13
Güver T., Özel F., 2009, MNRAS, 400, 2050 (LO09)
Hankins M., Lau R., Morris M., Herter T., 2017, ApJ, 837, 79
Heard V., Warwick R. S., 2013a, MNRAS, 428, 3462
Heard V., Warwick R. S., 2013b, MNRAS, 434, 1339
Heinke C. O., Tomsick J. A., Yusef-Zadeh F., Grindlay J. E., 2009, ApJ, 701, 1627
Heinz S. et al., 2015, ApJ, 806, 265
Heinz S., Corrales L., Smith R., Brandt W. N., Jonker P. G., Plotkin R. M., Neilsen J., 2016, ApJ, 825, 15
Henshaw J. D. et al., 2016, MNRAS, 457, 2675
Heyer M., Dame T. M., 2015, ARA&A, 53, 583
Hyodo Y., Ueda Y., Yuasa T., Maeda Y., Makishima K., Koyama K., 2009, PASJ, 61, S99
Jackson J. M. et al., 2006, ApJS, 163, 145
Jansen F. et al., 2001, A&A, 365, L1
Kennea J. A., Skinner G. K., 1996, PASJ, 48, L117
Kennea J. A. et al., 2013, ApJ, 770, L24
Kubryk M., Prantzos N., Athanassoula E., 2015, A&A, 580, A127
Kuulkers E., den Hartog P. R., in't Zand J. J. M., Verbunt F. W. M., Harris W. E., Cocchi M., 2003, A&A, 399, 663
Langer W. D., Goldsmith P. F., Pineda J. L., Velusamy T., Requena-Torres M. A., Wiesemeyer H., 2015, A&A, 576, A1
Leccardi A., Molendi S., 2008, A&A, 486, 359
Li A., Draine B. T., 2001, ApJ, 554, 778
McCollough M. L., Smith R. K., Valencic L. A., 2013, ApJ, 762, 2
Maeda Y., Koyama K., Sakano M., Takeshima T., Yamauchi S., 1996, PASJ, 48, 417
Mao J., Ling Z., Zhang S. N., 2014, ApJ, 785, 23
Markwardt C. B., 2009, in Bohlender D. A., Durand D., Dowler P., eds, ASP Conf. Ser. Vol. 411, Astronomical Data Analysis Software and Systems XVIII. Astron. Soc. Pac., San Francisco, p. 251
Marshall D. J., Joncas G., Jones A. P., 2009, ApJ, 706, 727
Mathis J. S., Lee C. W., 1991, ApJ, 376, 490
Mathis J. S., Rumpl W., Nordsieck K. H., 1977, ApJ, 217, 425 (MRN77)
Mezger P. G., Duschl W. J., Zylka R., 1996, A&AR, 7, 289
Molinari S. et al., 2011, ApJ, 735, L33
Mori K. et al., 2013, ApJ, 770, L23
Morris M., Serabyn E., 1996, ARA&A, 34, 645
Morrison R., McCammon D., 1983, ApJ, 270, 119
Muno M. P. et al., 2003, ApJ, 589, 225
Muno M. P. et al., 2005, ApJ, 622, L113
Muno M. P., Bauer F. E., Baganoff F. K., Brandt W. N., Ghez A., Lu J., Morris M. R., 2009, ApJS, 181, 110
Nakanishi H., Sofue Y., 2016, PASJ, 68, 5
Nieva M. F., Przybilla N., 2012, A&A, 539, A143
Nowak M. A. et al., 2012, ApJ, 759, 95
Overbeck J. W., 1965, ApJ, 141, 864
Paizis A. et al., 2015, ApJ, 808, 34
Peretto N., Fuller G. A., 2010, ApJ, 723, 555
Ponti G., Morris M. R., Terrier R., Goldwurm A., 2013, in Reimer O., Torres D. F., eds, Astrophysics and Space Science Proceedings, Vol. 34, Cosmic Rays in Star-Forming Environments. Springer-Verlag, Berlin Heidelberg, p. 331
Ponti G. et al., 2015a, MNRAS, 446, 1536
Ponti G. et al., 2015b, MNRAS, 453, 172
Ponti G. et al., 2016, MNRAS, 461, 2688
Ponti G., De K., Muñoz-Darias T., Stella L., Nandra K., 2017a, MNRAS, 464, 840
Ponti G. et al., 2017b, preprint (arXiv:1703.03410)
Porquet D. et al., 2008, A&A, 488, 549
Predehl P., Schmitt J. H. M. M., 1995, A&A, 293, 889
Predehl P., Schmitt J. H. M. M., Snowden S. L., Truemper J., 1992, Science, 257, 935
Rea N. et al., 2013, ApJ, 775, L34
Read A. M., Rosen S. R., Saxton R. D., Ramirez J., 2011, A&A, 534, A34
Reid M. J. et al., 2009, ApJ, 700, 137
Reynolds M., Kennea J., Degenaar N., Wijnands R., Miller J., 2016, Astron. Telegram, 8649
Rolf D. P., 1983, Nature, 302, 46
Roman-Duval J., Jackson J. M., Heyer M., Rathborne J., Simon R., 2010, ApJ, 723, 492
Sato M. et al., 2014, ApJ, 793, 72
Schultheis M. et al., 2014, A&A, 566, A120
Serabyn E., Guesten R., 1987, A&A, 184, 133
Seward F. D., Smith R. K., 2013, ApJ, 769, 17
Shannon R. M., Johnston S., 2013, MNRAS, 435, L29
Sicheneder E., Dexter J., 2017, MNRAS, 467, 3642
Simon R., Rathborne J. M., Shah R. Y., Jackson J. M., Chambers E. T., 2006, ApJ, 653, 1325
Smith R. K., 2008, ApJ, 681, 343
Smith R. K., Edgar R. J., Shafer R. A., 2002, ApJ, 581, 562
Smith R. K., Valencic L. A., Corrales L., 2016, ApJ, 818, 143
Snowden S. L., Kuntz K. D., 2011, BAAS, 43, 344.17
Spitler L. G. et al., 2014, ApJ, 780, L3
Tan J. C., Draine B. T., 2004, ApJ, 606, 296
Terrier R. et al., 2010, ApJ, 719, 143
Tremaine S. et al., 2002, ApJ, 574, 740
Trümper J., Schönfelder V., 1973, A&A, 25, 445
Ueda Y. et al., 2010, ApJ, 713, 257
Urban O., Werner N., Simionescu A., Allen S. W., Böhringer H., 2011, MNRAS, 414, 2101
Valencic L. A., Smith R. K., 2008, ApJ, 672, 984
Valencic L. A., Smith R. K., 2015, ApJ, 809, 66 (VS15)
Valencic L. A., Smith R. K., Dwek E., Graessle D., Dame T. M., 2009, ApJ, 692, 502
Vallée J. P., 2014, AJ, 148, 5
Vasilopoulos G., Petropoulou M., 2016, MNRAS, 455, 4426
Verner D. A., Ferland G. J., Korista K. T., Yakovlev D. G., 1996, ApJ, 465, 487
Voshchinnikov N. V., Henning T., Il'in V. B., 2017, ApJ, 837, 25
Wang Q. D., Gotthelf E. V., Lang C. C., 2002, Nature, 415, 148
Weingartner J. C., Draine B. T., 2001, ApJ, 548, 296 (WD01)
Williams M. J., Bureau M., Cappellari M., 2010, MNRAS, 409, 1330
Wilms J., Allen A., McCray R., 2000, ApJ, 542, 914 (WAM00)
Wucknitz O., 2015, preprint (arXiv:1501.04510)
Xiang J., Zhang S. N., Yao Y., 2005, ApJ, 628, 769
Xiang J., Lee J. C., Nowak M. A., 2007, ApJ, 660, 1309
Xiang J., Lee J. C., Nowak M. A., Wilms J., 2011, ApJ, 738, 78
Xu Y., McCray R., Kelley R., 1986, Nature, 319, 652
Zhang S. et al., 2015, ApJ, 815, 132
Zubko V., Dwek E., Arendt R. G., 2004, ApJS, 152, 211 (ZDA04)

Downloaded from https://academic.oup.com/mnras/article/468/3/2532/3072846 by Biblioteca di Scienze tecnologiche user on 30 December 2020

APPENDIX A: COMBINED RADIAL PROFILES OF AX J1745.6−2901 AND THE BACKGROUND EMISSION

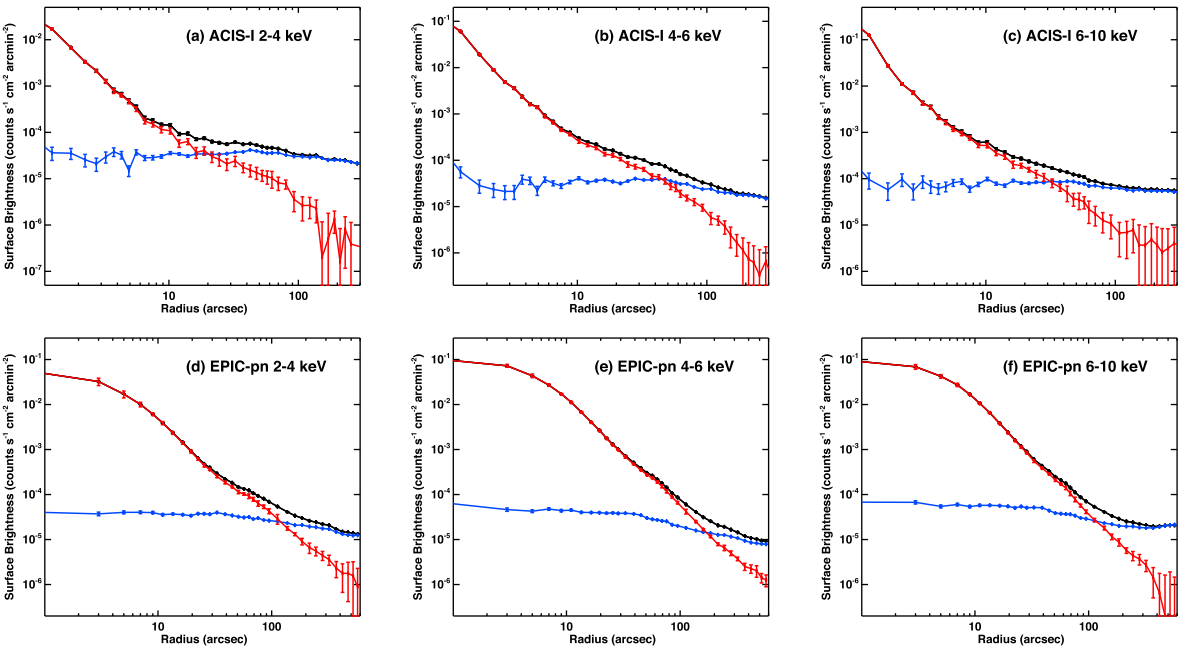


Figure A1. Combined radial profiles of AX J1745.6−2901 in *Chandra* and *XMM–Newton* in three energy bands before background subtraction (black) and after (red). The blue data points show the radial profile of the diffuse emission plus detector background as measured during quiescent periods of AX J1745.6−2901.

APPENDIX B: LIST OF BACKGROUND OBSERVATIONS

Table B1. List of *XMM–Newton* and *Chandra* observations used to determine the emission underneath the halo of AX J1745.6−2901 when it was in the quiescent state (i.e. detector background plus diffuse emission). 'Exp' and 'CL-Exp' are the total exposure time and clean exposure time without background flares. $\theta_{\rm off}$ is the off-axis angle of AX J1745.6−2901.

Chandra ObsID	Start-Time	Target	ACIS-Grating	Exp (ks)	CL-Exp (ks)	$\theta_{\rm off}$ (arcmin)
242	1999-09-21	Sgr A*	ACIS-I (None)	45.9	42.2	1.45
2943	2002-05-22	Sgr A*	ACIS-I (None)	37.7	37.7	1.45
3663	2002-05-24	Sgr A*	ACIS-I (None)	38.0	38.0	1.45
4683	2004-07-05	Sgr A*	ACIS-I (None)	49.5	49.5	1.45
4684	2004-07-06	Sgr A*	ACIS-I (None)	49.5	49.5	1.45
5950	2005-07-24	Sgr A*	ACIS-I (None)	48.5	48.5	1.45
5951	2005-07-27	Sgr A*	ACIS-I (None)	44.6	44.6	1.45
5952	2005-07-29	Sgr A*	ACIS-I (None)	45.3	43.5	1.45
5953	2005-07-30	Sgr A*	ACIS-I (None)	45.4	45.4	1.45
5954	2005-08-01	Sgr A*	ACIS-I (None)	17.9	17.9	1.45
6363	2006-07-17	Sgr A*	ACIS-I (None)	29.8	29.8	1.45
10556	2009-05-18	Sgr A*	ACIS-I (None)	112.5	112.5	1.45
11843	2010-05-13	Sgr A*	ACIS-I (None)	78.9	78.9	1.45
13016	2011-03-29	Sgr A*	ACIS-I (None)	17.8	17.8	1.45
13017	2011-03-31	Sgr A*	ACIS-I (None)	17.8	17.8	1.45
14941	2013-04-06	Sgr A*	ACIS-I (None)	19.8	19.8	1.45
14942	2013-04-14	Sgr A*	ACIS-I (None)	19.8	19.8	1.45
combined	–	–	–	718.8	713.3	–

Downloaded from https://academic.oup.com/mnras/article/468/3/2532/3072846 by Biblioteca di Scienze tecnologiche user on 30 December 2020

Table B1 – *continued.*

Chandra ObsID	Start-Time	Target	ACIS-Grating	Exp (ks)	CL-Exp (ks)	$\theta_{\rm off}$ (arcmin)
13850	2012-02-10	Sgr A⋆	ACIS-S (HETG)	59.3	59.0	1.45
14392	2012-02-11	Sgr A⋆	ACIS-S (HETG)	58.4	58.0	1.45
14394	2012-02-10	Sgr A⋆	ACIS-S (HETG)	17.8	17.8	1.45
14393	2012-02-11	Sgr A⋆	ACIS-S (HETG)	41.0	40.9	1.45
13856	2012-03-15	Sgr A⋆	ACIS-S (HETG)	39.5	39.3	1.45
13857	2012-03-17	Sgr A⋆	ACIS-S (HETG)	39.0	39.0	1.45
13854	2012-03-20	Sgr A⋆	ACIS-S (HETG)	22.8	22.5	1.45
14414	2012-03-23	Sgr A⋆	ACIS-S (HETG)	19.8	19.8	1.45
14427	2012-05-06	Sgr A⋆	ACIS-S (HETG)	79.0	79.0	1.45
13848	2012-05-09	Sgr A⋆	ACIS-S (HETG)	96.9	96.9	1.45
13849	2012-05-11	Sgr A⋆	ACIS-S (HETG)	176.4	176.4	1.45
13846	2012-05-16	Sgr A⋆	ACIS-S (HETG)	55.5	54.0	1.45
combined	–	–	–	705.5	702.7	–
XMM–Newton ObsID	Start-Time	Target	pn-Filter	Exp (ks)	CL-Exp (ks)	$\theta_{\rm off}$ (arcmin)
0554750401	2009-04-01	Sgr A⋆	PFW-Medium	39.9	32.0	1.46
0554750501	2009-04-03	Sgr A⋆	PFW-Medium	44.3	38.1	1.46
0554750601	2009-04-05	Sgr A⋆	PFW-Medium	39.1	31.8	1.46
0604300601	2011-03-28	Sgr A⋆	PFW-Medium	48.8	27.3	1.46
0604300801	2011-04-01	Sgr A⋆	PFW-Medium	48.8	33.9	1.46
0604300901	2011-04-03	Sgr A⋆	PFW-Medium	46.9	18.8	1.46
0604301001	2011-04-05	Sgr A⋆	PFW-Medium	50.7	27.6	1.46
0658600101	2011-08-31	Sgr A⋆	PFW-Medium	49.9	48.1	1.51
0658600201	2011-09-01	Sgr A⋆	PFW-Medium	53.2	39.3	1.51
0674600601	2012-03-13	Sgr A⋆	PFW-Medium	21.5	8.4	1.46
0674600701	2012-03-15	Sgr A⋆	PFW-Medium	15.9	7.0	1.46
0674601101	2012-03-17	Sgr A⋆	PFW-Medium	28.0	10.6	1.46
0674600801	2012-03-19	Sgr A⋆	PFW-Medium	22.9	16.0	1.46
0674601001	2012-03-21	Sgr A⋆	PFW-Medium	23.9	19.4	1.46
combined	–	–	–	358.3	332.1	–

This paper has been typeset from a TEX/LATEX file prepared by the author.

Downloaded from https://academic.oup.com/mnras/article/468/3/2532/3072846 by Biblioteca di Scienze tecnologiche user on 30 December 2020